Secondary aerosol formation ~~Fine particle chemistry~~ under a special dust transport event: impacts from unusually enhanced ozone and ~~air mass~~dust backflows over the ocean

Da Lu[1], Hao Li[1], Guochen Wang[1], Xiaofei Qin[1], Na Zhao[1], Juntao Huo[2], Fan Yang[3], Yanfen Lin[2], Jia Chen[2], Qingyan Fu[2], Yusen Duan[2], Xinyi Dong[4], Congrui Deng[1], Sabur F. Abdullaev[5], Kan Huang[1,6*]

[1]Center for Atmospheric Chemistry Study, Shanghai Key Laboratory of Atmospheric Particle Pollution and Prevention (LAP[3]), National Observations and Research Station for Wetland Ecosystems of the Yangtze Estuary, Department of Environmental Science and Engineering, Fudan University, Shanghai, 200433, China

[2]State Ecologic Environmental Scientific Observation and Research Station for Dianshan Lake, Shanghai Environmental Monitoring Center, Shanghai, 200030, China

[3]Pudong New District Environmental Monitoring Station, Shanghai 200122, China

[4]School of Atmospheric Sciences, Nanjing University, Nanjing 210023, China

[5]Physical Technical Institute of the Academy of Sciences of Tajikistan, Dushanbe, Tajikistan

[6]Institute of Eco-Chongming (IEC), Shanghai, 202162, China

Corresponding author: huangkan@fudan.edu.cn

Abstract

In the autumn of 2019, ~~A~~ a five-day~~s~~ long-lasting dust event was observed ~~with~~ using a synergy of field measurement~~s~~ techniques in Shanghai ~~in the autumn of 2019~~.

This particular dust event stood out from others due to its unique characteristics. ~~Different from most dust events, this dust was an unusual one characterized of~~ including low wind speed, high relative humidity, elevated levels~~high concentrations~~ of gaseous precursors, and contrasting wind patterns at different altitudes~~vectors between low and high altitudes~~. During this event, three distinct dust stages were identified. ~~Three dust stages were identified and t~~The first stage was a typical ~~normal~~ dust invasion characterized by with high concentrations of particulate matters ~~concentrations and~~ but relatively short duration. In contrast, the second stage exhibited an unusual enhancement of ozone ~~was observed in the second stage~~, attributed ~~due~~ to compound causes of weak synoptic system, transport from the ocean, and subsidence of high-altitude ozone~~O_3~~ down drafted by dust. Consequently~~As a result~~, gas phase oxidation served as the major formation pathway of sulfate and nitrate ~~moderately correlated with O_3 while had almost no correlation with aerosol liquid water content, indicating the dominant role of gas phase oxidations~~. ~~During~~ In the third stage of dust, a noteworthy phenomenon known as dust backflow occurred. ~~a special phenomenon of dust backflow was observed that t~~The dust plume originated ~~drifted~~ from the Shandong Peninsula and slowly drifted~~travelled slowly~~ over the Yellow Sea and the East China Sea before eventually~~, finally~~ returning to Shanghai. Evidence of this ~~The dust~~ backflow was found through~~evidenced by~~ the enrichment of marine vessel emissions (V and Ni) and increased solubility of calcium. Under the influence of humid oceanic breezes, the formation of nitrate was dominated by aqueous processing. Additionally, part of nitrate and sulfate were ~~, while the strong correlation between SO_4^{2-} and Na^+ suggested that a considerable part of sulfate was aged and~~ directly transported via sea salts, evidenced by ~~,~~their co-variation with Na^+ and confirmed through ~~Based on the~~ thermodynamic

Formatted: Font: (Default) Times New Roman, 小四, Font color: Auto, Pattern: Clear

Formatted: Font: (Default) Times New Roman, 小四, Font color: Auto, Pattern: Clear

Formatted: Font: (Default) Times New Roman, 小四, Font color: Auto, Pattern: Clear

Formatted: Font: (Default) Times New Roman, 小四, Font color: Auto, Pattern: Clear

Formatted: Font: (Default) Times New Roman, 小四, Font color: Auto, Pattern: Clear

Formatted: Font: (Default) Times New Roman, 小四, Font color: Auto, Pattern: Clear

Formatted: Font: (Default) Times New Roman, 小四, Font color: Auto, Pattern: Clear

Formatted: Font: (Default) Times New Roman, 小四, Font color: Auto, Pattern: Clear

Formatted: Font color: Text 1

Formatted: Font: (Default) Times New Roman, 小四, Font color: Text 1, Pattern: Clear

Formatted: Font: (Default) Times New Roman, 小四, Font color: Auto, Pattern: Clear

Formatted: Font: (Default) Times New Roman, 小四, Font color: Auto, Pattern: Clear

Formatted: Font: (Default) Times New Roman, 小四, Font color: Auto, Pattern: Clear

Formatted: Font: (Default) Times New Roman, 小四, Font color: Auto, Pattern: Clear

Formatted: Font: (Default) Times New Roman, 小四, Font color: Auto, Pattern: Clear

Formatted: Font: (Default) Times New Roman, 小四, Font color: Auto, Pattern: Clear

Formatted: Font: (Default) Times New Roman, 小四, Font color: Auto, Pattern: Clear

Formatted: Font: (Default) Times New Roman, 小四, Font color: Auto, Pattern: Clear

modeling~~, sea salts probably involved more in the secondary aerosol formation than the dust heterogeneous reactions~~. The uptake of NH_3 on particles, influenced by the contributions of alkali metal ions and aerosol pH, regulated the formation potential of secondary aerosol. By developing an upstream-receptor relationship method, the amounts of transported and secondarily formed aerosol species were separated. This study highlights that the transport pathway of dust, coupled with ~~and~~ environmental conditions, ~~could~~ can significantly modify the aerosol properties, especially at the complex land-sea interface.

1. Introduction

Dust serves as a significant natural source of aerosols, constituting approximately~~As an important source of natural aerosols, dust accounted for about~~ half of the tropospheric aerosols (Zheng et al., 2016). Dust aerosols play~~ed~~ crucial ~~important~~ roles in environmental and climatic changes by affecting the radiation balance (Feng et al., 2020; Nagashima et al., 2016; Goodman et al., 2019). The optical properties of dust aerosols are influenced by various parameters of iron oxides, including refractive indices, size distributions, and mineralogical compositions. Consequently, these factors introduce potential uncertainties regarding the role of dust in climate forcing (Zhang et al., 2015; Jeong, 2008). Furthermore, dust aerosols have ~~had~~ important impacts ~~influences~~ on tropospheric chemistry by participating in heterogeneous and photolysis reactions in the atmosphere (Wang et al., 2014; Liu et al., 2018). During transport~~For instance~~, dust ~~could~~ can mix with gaseous pollutants, toxic metals, and soot ~~during transport~~, thereby ~~thus~~ affecting air quality immediately and potentially posing~~causing potential~~ public health hazards (Liu et al., 2021; Wang et al., 2021). Moreover, Barkley

Formatted: Subscript

Formatted: Font: (Default) Times New Roman, 小四, Font color: Auto, Pattern: Clear

Formatted: Font: (Default) Times New Roman, 小四, Font color: Auto, Pattern: Clear

Formatted: Font: (Default) Times New Roman, 小四, Font color: Auto, Pattern: Clear

Formatted: Font: (Default) Times New Roman, 小四, Font color: Auto, Pattern: Clear

Formatted: Font: (Default) Times New Roman, 小四, Font color: Auto, Pattern: Clear

Formatted: Font: (Default) Times New Roman, 小四, Font color: Auto, Pattern: Clear

Formatted: Font: (Default) Times New Roman, 小四, Font color: Auto, Pattern: Clear

Formatted: Font: (Default) Times New Roman, 小四, Font color: Auto, Pattern: Clear

Formatted: Font: (Default) Times New Roman, 小四, Font color: Auto, Pattern: Clear

et al. (2021) found that iron-containing aerosols transported from Africa to the equatorial North Atlantic Ocean provided plentiful nutrients to algae in the ocean and accumulated inside algae.

~~Many studies focused on the emissions and transport of Asian dust, which accounted for ~ 20% of the global dust budget (Ginoux et al., 2004). Asian dust mostly originated from the deserts in western China, the Gobi, and the Loess Plateau (Nagashima et al., 2016). Dust particles can be lifted to an altitude of several kilometers due to strong winds and low soil moistures. During this process, most of the coarse dust particles would settle near the dust source areas, while relatively fine particles could be transported to further downstream regions such as eastern and southern China, and even across the Pacific Ocean to the western America coast~ (Huang et al., 2010b; Vicars and Sickman, 2011)~~.

~~–~~The irregular shapes of dust particles provide~~d~~ an ~~–~~efficient medium for heterogeneous reactions with NO_2, O_3, SO_2, and NH_3, thereby altering~~thus changing~~ the particle size spectrum, hygroscopicity, and radiative properties (Hsu et al., 2014; Tian et al., 2021; Jiang et al., 2018). Jiang et al. (2018) observed a significant increase ~~that the concentrations of~~in nitrate and sulfate concentrations during a dust period in March 2010 in Shanghai. This elevation was attributed ~~were significantly elevated due~~ to the presence of moderate~~/~~ to high levels of relative humidity and gaseous precursors ~~during a dust period in March, 2010 at Shanghai~~, implying that dust can efficiently promote~~d~~ the formation of sulfate and nitrate. ~~The formation of nitrate included two major pathways. During daytime, the OH radicals produced by the photolysis of O_3 and HONO oxidized NO_2 to produce HNO_3 (Hertel et al., 2012), which subsequently neutralized the alkaline substances to form nitrate in the particles. During nighttime~~

Formatted: Font: (Default) Times New Roman, 小四, Font color: Auto, Pattern: Clear

Formatted: Font: (Default) Times New Roman, 小四, Font color: Auto, Pattern: Clear

Formatted: Font: (Default) Times New Roman, 小四, Font color: Auto, Pattern: Clear

Formatted: Font: (Default) Times New Roman, 小四, Font color: Auto, Pattern: Clear

~~with low temperature and high humidity, NO_2 can be oxidized by O_3 to form NO_3 radical (Mentel et al., 1996), which then reacted with NO_2 to form N_2O_5 radical (Dall'osto et al., 2009; Petetin et al., 2016).~~ Previous studies have revealed that HNO_3 formed through the reactions of NO_2 with hydroxyl radical or N_2O_5 hydrolysis ~~would~~ preferentially react**s** with mineral dust particles and produce nitrate, which serves as the primary~~was the main~~ source of nitrate during ~~the~~ dust ~~period~~ episodes (Tang et al., 2016; Wu et al., 2020). Improvements in the simulation of sulfate were achieved by employing various parameterization schemes for the heterogeneous uptake of SO_2 on natural dust surfaces in the presence of NH_3 and NO_2 under different relative humidity conditions(Zhang et al., 2019)~~.~~ Wang et al. (2018) ~~found~~ simulated that ~~the~~ heterogeneous reactions on ~~the~~ dust ~~surface were the main sources~~accounted for the majority of nitrate~~, and the dust surface nitrate observed in Japan mainly formed~~ over the Yellow Sea and the East China Sea during the dust long-range transport. Tang et al. (2017) conducted a comprehensive review on the effect of dust heterogeneous reactions on the tropospheric oxidation capacity. They proposed that high RH (> 80%) and a wider range of temperature should be considered in the laboratory studies of heterogeneous reactions of mineral dust. Additionally, more comprehensive kinetic models should be developed to understand the complex multiphase reactions.

Controversies have arisen regarding~~However, there were some controversies on~~ the mixing of dust and anthropogenic aerosols. Zhang et al. (2005) found that anthropogenic aerosols separated with dust during a dust event in Qingdao, China. Coincidentally, ~~there existed~~ a time-lag between dust and anthropogenic aerosols was observed in Japan and South Korea downstream of the dust transport. Single particle analysis revealed ~~confirmed~~ that sulfate in fine particles appeared 12 hours before the

Formatted: Font: (Default) Times New Roman, 小四, Font color: Auto, Pattern: Clear

Formatted: Font: (Default) Times New Roman, 小四, Font color: Auto, Pattern: Clear

Formatted: Font: (Default) Times New Roman, 小四, Font color: Auto, Subscript, Pattern: Clear

Formatted: Font: (Default) Times New Roman, 小四, Font color: Auto, Pattern: Clear

Formatted: Font: (Default) Times New Roman, 小四, Font color: Auto, Subscript, Pattern: Clear

Formatted: Font: (Default) Times New Roman, 小四, Font color: Auto, Pattern: Clear

Formatted: Font: (Default) Times New Roman, 小四, Font color: Auto, Subscript, Pattern: Clear

Formatted: Font: (Default) Times New Roman, 小四, Font color: Auto, Pattern: Clear

Formatted: Font: (Default) Times New Roman, 小四, Font color: Auto, Pattern: Clear

Formatted: Font: (Default) Times New Roman, 小四, Font color: Auto, Pattern: Clear

Formatted: Font: (Default) Times New Roman, 小四, Font color: Auto, Pattern: Clear

dust arrival in Japan. Wang et al. (2013) also observed a lag of 10 - 12 hours ~~lag~~ between dust and anthropogenic aerosols ~~in~~ on a dust day in Shanghai (Wang et al., 2013). Furthermore, Huang et al. (2019) documented vertical differences in~~observed that there were vertical differences of the~~ long-transported aerosols during a pollution event in Taiwan. Dust from the Gobi Desert in Inner Mongolia and China existed at the altitudes of 0.8km and 1.90km, respectively, while biomass burning aerosols from South Asia were present~~existed~~ at higher altitudes of 3.5km. Coastal regions often experience a mixture of inland anthropogenic emissions and releases from the ocean, making regional pollution complex in these areas ~~In the coastal regions, the regional pollution was always a mix of inland anthropogenic emissions and ocean-sourced releases. Due to the active human activities and special weather conditions such as monsoon and sea-land breezes, the atmospheric compound pollution was usually more complex in the coastal areas~~ (Wang et al.; Hilario et al., 2020; Patel and Rastogi, 2020; Perez et al., 2016; Wang et al., 2017). The eastern coast of China, ~~is~~ bordering the East China Sea and the Yellow Sea, ~~and~~ is particularly ~~strongly~~ influenced by the Asian monsoon and high emissions from inland industries, resulting in highly intricate~~. The~~ meteorological ~~conditions~~ and pollution conditions ~~in this region were among the most complex in the world~~ (Hilario et al., 2020). Furthermore, the marine boundary layer in this region exhibits significant seasonal and diurnal variations in ~~Due to the complex meteorological conditions, the~~ relative humidity and temperature ~~of the marine boundary layer showed significant seasonal and diurnal changes,~~ further impacting ~~affecting the~~ photochemical processes and ~~the~~ heterogeneous reactions on ~~the~~ aerosol surfaces (Zhao et al., 2021). Sea and land breezes play a crucial role in this coastal area. During the night, land breezes carry

Formatted: Font: (Default) Times New Roman, 小四, Font color: Auto, Pattern: Clear

pollutants from the land to the sea. Subsequently, during the day, these land breezes transform into sea breezes, bringing the pollutants back over the sea. This phenomenon leads to an increase in air pollutants over the land~~Under the influence of sea and land breezes, land breezes at night blew the land pollutants to the sea. In the next day, land breezes would evolve as sea breezes and return the pollutants over the sea to the land, resulting in the increase of air pollutants over the land~~ (Zhao et al., 2021). For instance~~Meanwhile~~, Wang et al. (2022b) found that during the ozone pollution in Shanghai in 2018, the presence of O_3 at high altitudes at night was transported vertically downward during the daytime and high O_3 over the ocean was transported horizontally to the land, ~~thus~~ jointly ~~causing~~contributing to regional O_3 pollution in Shanghai. Also, one dust episode in 2014 was observed over Shanghai via detouring from northern China due to the blocked north Pacific subtropical high-pressure system (Wang et al., 2018).

~~High relative humidity caused by the sea breeze favored the participation of gaseous precursors in heterogeneous reactions, hygroscopic growth of particles, and secondary aerosol formation. Sun et al. (2020) found that nitrate was the main species of aerosol in Shanghai during pollution events from 2017-2018, while most of these events in winter were caused by the long transport of air pollutants from the North China Plain. Sea salt, as an important component of aerosol in coastal areas, has been found in various studies that complex multiphase reactions can occur on the surface of sea salts~~ (Huang et al., 2010b; Patel and Rastogi, 2020; Wang et al., 2022a)~~. Wang et al. (2022a) found that the addition of Na^+ in the ISORROPIA model improved the simulation performance of aerosol and gaseous species at a coastal site in the South China Sea, indicating that sea salts participated in the heterogeneous reactions with other aerosol~~

Field Code Changed

Formatted: Not Highlight

Formatted: Indent: First line: 0 ch

~~species. Liang et al. (2018) found that the rise of O_3 in Shanghai could be affected by both local secondary formation and marine transport based on observation and simulation. Meanwhile, Wang et al. (2022b) found that during the ozone pollution in Shanghai in 2018, the presence of O_3 at high altitudes at night was transported vertically downward during the daytime and high O_3 over the ocean was transported horizontally to the land, thus jointly causing regional O_3 pollution in Shanghai.~~

Previous studies have shown that about 70% of Asian dust traverses ~~would pass through~~ the eastern coast of China before ~~and then~~ moving towards the~~moved out over~~ Korean Peninsula, ~~and~~ the Sea of Japan, and eventually reaching ~~finally ending at~~ the Pacific Ocean. The eastern coast of China serves as a crucial~~is considered as the essential~~ route ~~of~~ for ~~the~~ Asian dust transport to the Pacific Ocean (Arimoto et al., 1997; Huang et al., 2010a). Most previous research has focused on typical dust events characterized by strong intensities, high wind speed, low humidity, and low oxidants (Li et al., 2017; Ma et al., 2019; Xu et al., 2017; Xie et al., 2005). ~~In t~~ In contrast, this study aims to depict~~,~~ an atypical dust event was observed in Shanghai, a coastal mega-city in Eastern China. The unusualness of the meteorological conditions, transport pathways, and air pollutants during the particular dust event was explicitly described. The study involves categorizing the dust event into t~~T~~hree stages ~~of the dust were sorted~~ and comparing the aerosol chemical compositions between these stages. ~~were compared.~~ By focusing on the second and third stages, the different formation mechanisms of nitrate and sulfate were investigated. The amounts of major aerosol species from transport and secondary formation were estimated based on a simplified ~~simple~~ method of relating the upstream and receptor simultaneous measurements.

Formatted: Font: (Default) Times New Roman, 小四, Font color: Auto, Pattern: Clear

Formatted: Font: (Default) Times New Roman, 小四, Font color: Auto, Pattern: Clear

Formatted: Font: (Default) Times New Roman, 小四, Font color: Auto, Pattern: Clear

Formatted: Font: (Default) Times New Roman, 小四, Font color: Auto, Pattern: Clear

Formatted: Font: (Default) Times New Roman, 小四, Font color: Auto, Pattern: Clear

Formatted: Font: (Default) Times New Roman, 小四, Font color: Auto, Pattern: Clear

Formatted: Font: (Default) Times New Roman, 小四, Font color: Auto, Pattern: Clear

Formatted: Font: (Default) Times New Roman, 小四, Font color: Auto, Pattern: Clear

Formatted: Font: (Default) Times New Roman, 小四, Font color: Auto, Pattern: Clear

Formatted: Font color: Auto

2. Methodology

2.1. Observational sites

~~Measurements of various atmospheric parameters were conducted~~ A~~a~~t Shanghai Pudong Environmental Monitoring Station (31°13′N, 121°32′E), comprehensive measurements of various atmospheric parameters were conducted. All the instruments were installed ~~set up~~ on the top floor of ~~the~~ a building, about 25m above the ground level. As shown in Figure S1, the sampling site ~~was~~ is situated ~~located~~ at the eastern tip of Shanghai, close to the coastal line. During November, ~~The~~ the mean temperature and relative humidity in Shanghai were recorded as 17.3℃ and 72% ~~in Shanghai during November,~~ respectively. In autumn and winter, air pollutants originating from upstream urban regions often undergo ~~could be frequently~~ transport~~ed~~ to Shanghai via ~~the~~ high-pressure system~~s~~. Additionally~~Furthermore~~, air pollutants in Shanghai tended to linger at the sea/land boundary regions due to the sea-land breeze (Shen et al., 2019).

In addition to the measurements taken in Shanghai, data from environmental monitoring stations in Qingdao and Lianyungang are also incorporated into~~used in~~ this study.

Formatted: Font: (Default) Times New Roman, 小四, Font color: Auto, Pattern: Clear

Formatted: Font: (Default) Times New Roman, 小四, Font color: Auto, Pattern: Clear

Formatted: Font: (Default) Times New Roman, 小四, Font color: Auto, Pattern: Clear

Formatted: Font: 小四

Formatted: Font: (Default) Times New Roman, 小四, Font color: Auto, Pattern: Clear

Formatted: Font: (Default) Times New Roman, 小四, Font color: Auto, Pattern: Clear

Formatted: Font: (Default) Times New Roman, 小四, Font color: Auto, Pattern: Clear

Formatted: Font: (Default) Times New Roman, 小四, Font color: Auto, Pattern: Clear

Formatted: Font: (Default) Times New Roman, 小四, Font color: Auto, Pattern: Clear

Formatted: Font: (Default) Times New Roman, 小四, Font color: Auto, Pattern: Clear

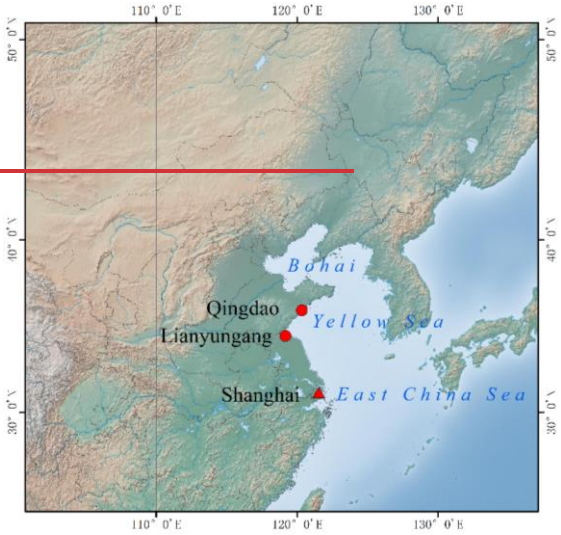

~~Figure 1. The observational sites in this study, including Shanghai, Qingdao, and Lianyungang.~~

2.2. Instrumentation

A set of online instruments was set up at the Pudong observational site. Inorganic ions (NO_3^-, SO_4^{2-}, Cl^-, Na^+, NH_4^+, K^+, Mg^{2+}, Ca^{2+}) in $PM_{2.5}$ and soluble gases (NH_3, HNO_3, HCl, HONO) were measured by an online ion chromatography (IC, MARGA-1S, Metrohm). It operated at a flow rate of 16.7 L/min with a time resolution of one hour. Briefly, air was drawn into a $PM_{2.5}$ cyclone inlet and passed through a wet rotating denuder (gases) and a steam jet aerosol collector (aerosols). Subsequently, the aqueous samples were analyzed with ion chromatography. More details can be found in (Xu et al., 2020). Hourly trace metals (Si, Ca, Cu, Fe, K, Co, Mn, Cr, Zn, Pb, As, Cd, V, Ni) in $PM_{2.5}$ were measured by using the Xact 625 multi-metals monitor (Cooper Environmental, Beaverton, OR, USA). Particles were collected onto a Teflon filter tape at a flow rate of 16.7 L/min, and then transported into the spectrometer where the

Formatted: Justified, Indent: First line: 0 ch

particles were analyzed with an X-ray fluorescence. Organic carbon and elemental carbon were measured by an in situ Semi-Continuous Organic Carbon and Elemental Carbon aerosol analyzer (RT-4, Sunset Laboratory, Beaverton, Oregon, USA). The concentration of mineral aerosols is calculated by summing the major mineral elements with oxygen for their normal oxides, i.e., [Minerals]= (2.2*Al+2.49*Si+1.63*Ca+2.42*Fe+1.94*Ti) (Malm et al., 1994). The concentration of OM (organic matters) is estimated by multiplying OC with a factor of 2.

The concentrations of particles and gaseous pollutants were measured by a set of Thermo Fisher Scientific instruments, including $PM_{2.5}$ (Thermo 5030i), PM_{10} (Thermo 5030i), SO_2 (Thermo Fisher 43i), NO_x (Thermo Fisher 42i), O_3 (Thermo Fisher 49i), and CO (Thermo Fisher 48i-TLE). Meteorological parameters (ambient temperature, relative humidity, wind speed, and wind direction) were obtained by a Vaisala Weather transmitter (WXT520). Other supplementary parameters such as the height of planetary boundary layer (PBL), vertical profiles of ozone and aerosol extinction were obtained by a ceilometer (CL31, Vaisala), ozone lidar (LIDAR-G-2000, WUXIZHONGKE), and aerosol lidar (AGJ, AIOFM), respectively.

2.3. Thermodynamic simulation of aerosol pH and aerosol liquid water content

The ISORROPIA II model is subject to the principle of minimizing the Gibbs energy of the multi-phase aerosol system, leading to a computationally intensive optimization problem (Song et al., 2018). ISORROPIA II calculates the aerosol pH, ALWC (aerosol liquid water content) and compositions of ammonia-sulfate-nitrate-chloride-sodium-calcium-potassium-magnesium in the thermodynamic equilibrium with gas-phase precursors. The performances and advantages of ISORROPIA over the usage of other

thermodynamic equilibrium codes has been assessed in numerous studies (Nenes et al., 1998; West et al., 1999; Ansari and Pandis, 1999; Yu et al., 2005). The ISORROPIA running in the forward mode at the metastable state was applied in this study.

2.4. Hybrid Single-Particle Lagrangian Integrated Trajectory Model

The HYSPLIT (Hybrid Single-Particle Lagrangian Integrated Trajectory) was used to compute the backward trajectories of the air parcels during the dust events. In this study, the HYSPLIT model was driven by meteorological data outputs from the Global Data Assimilation System (GDAS) (Su et al., 2015), which is available at ftp://arlftp.arlhq.noaa.gov/pub/archives/gdas1. Air mass trajectories were launched at different heights from the ground and a total duration of 48 hours simulation was conducted.

2.5. Calculation of uptake coefficient of NH_3 (γ_{NH_3}) on particles

NH_3, being the most abundant alkaline species in the atmosphere, plays a crucial role in acid neutralization and secondary aerosol formation. To assess the gas-particle partitioning of NH_3, the uptake coefficient of NH_3 (γ_{NH3}) on particles is calculated as below. Initially, the quasi-first-order reaction rate constant for heterogeneous conversion from NH_3 to NH_4^+ (k_{het}, s^{-1}) is calculated according to (Liu et al., 2022).

$$k_{het} = \frac{2(C_{NH_4^+,t_2} - C_{NH_4^+,t_1})}{(C_{NH_3,t_2} + C_{NH_3,t_1})(t_2 - t_1)}$$

k_{het} is only valid when c_{NH4+} increases, while c_{NH3} decreases assuming a constant emission rate from t_1 to t_2 (1 h in this study). Then, the uptake coefficient of NH_3 (γ_{NH3})

Formatted: Font: Bold
Formatted: Font: Bold, Subscript
Formatted: Font: Bold
Formatted: Font: Bold, Subscript
Formatted: Font: Bold
Formatted: Font: (Default) Times New Roman, 小四, Font color: Auto, Pattern: Clear
Formatted: Indent: Left: 0 cm, First line: 2 ch
Formatted: Left
Formatted: Font: (Default) Times New Roman, 小四, Font color: Auto, Pattern: Clear
Formatted: Superscript
Formatted: Subscript
Formatted: Superscript
Formatted: Indent: Left: 0 cm, First line: 2 ch
Formatted: Subscript
Formatted: Subscript
Formatted: Subscript
Formatted: Subscript
Formatted: Subscript

on particles can be calculated as below (Liu et al., 2022; Wang and Lu, 2016).

$$\gamma_{NH_3} = \frac{4k_{het}}{S\omega} = \frac{4k_{het}}{S\sqrt{\frac{8RT}{\pi M}}}$$

where S is the surface area of particles ($m^2\ m^{-3}$) measured using SMPS and APS. ω is the velocity of NH_3 molecules. T is the ambient temperature (K). R is the ideal gas constant, and M is the molecular weight of NH_3 ($kg\ mol^{-1}$).

3. Results and Discussion

3.1. Characteristics of an unusual dust event

~~Figure 2~~ Figure 1 shows the time series of PM_{10}, $PM_{2.5}$, ~~and~~ meteorological parameters, as well as the vertical profiles of aerosol extinction coefficient and depolarization ratio observed at the Shanghai sampling site from October 25 to November 6, 2019. ~~During~~ From October 25 to 28, the mean wind speed remained ~~was~~ relatively low of 0.9±0.72m/s with ~~the~~ a peak value of 3.1m/s, and predominantly blowing~~winds prevailed~~ from the northwest. The mean concentration of $PM_{2.5}$ and PM_{10} was 34.7 and 44.2 μg/m^3, respectively. Starting at 4:00 LST on October 29, the concentration of PM_{10} increased sharply and lasted till November 2 (Figure 1~~2~~d). ~~Based on the~~The aerosol lidar observation indicated that~~,~~ both the aerosol extinction coefficient and depolarization ratio extended from the ground to around 2km during the same period. Notably~~Specifically~~, the enhanced depolarization ratio (>0.1) suggested the occurrence of a prolonged dust event in Shanghai. ~~was obviously enhanced (>0.1), indicating that Shanghai encountered a long-lasting dust event.~~ Throughout the entire~~During the whole~~ dust period, the mean concentrations of $PM_{2.5}$ and PM_{10} reached 53.3 ± 20.5μg/m^3 and 172.4 ± 70.2μg/m^3, respectively, yielding a low $PM_{2.5}/PM_{10}$ ratio

Formatted: Superscript
Formatted: Indent: Left: 0 cm, First line: 0 cm
Formatted: Superscript
Formatted: Subscript
Formatted: Subscript
Formatted: Superscript
Formatted: Indent: Left: 0 cm, Hanging: 4.2 ch, First line: 0 ch
Formatted: Font: (Default) Times New Roman, 小四, Font color: Auto, Pattern: Clear
Formatted: Font: (Default) Times New Roman, 小四, Font color: Auto, Pattern: Clear
Formatted: Font: (Default) Times New Roman, 小四, Font color: Auto, Pattern: Clear
Formatted: Font: (Default) Times New Roman, 小四, Font color: Auto, Pattern: Clear
Formatted: Font: (Default) Times New Roman, 小四, Font color: Auto, Pattern: Clear

of 0.34 ± 0.15. As a comparison, $PM_{2.5}$ and PM_{10} during the non-dust period was 38.9μg/m^3 and 49.8μg/m^3, respectively, exhibiting ~~with~~ a relatively high $PM_{2.5}/PM_{10}$ ratio of 0.62 ± 0.20.

Formatted: Font: (Default) Times New Roman, 小四, Font color: Auto, Pattern: Clear

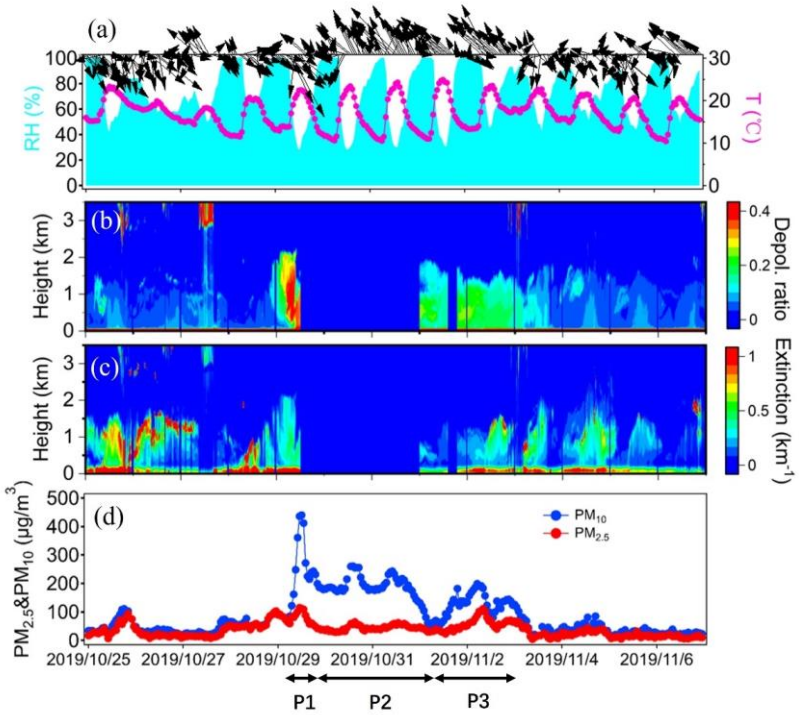

Figure 1~~2~~. Time series of (a) relative humidity, temperature, wind vectors, (b) aerosol depolarization ratio, (c) aerosol extinction coefficient, (d) mass concentrations of $PM_{2.5}$ and PM_{10} during the study period. Three dust stages, i.e., P1, P2, and P3 are also marked. The missing aerosol lidar data were due to instrument malfunction.

The occurrences of dust ~~were~~ are typically ~~usually~~ accompanied by low relative humidity and strong winds due to the passage of cold fronts (Huang et al., 2010b; Huang et al., 2010a; Wang et al., 2013; Wang et al., 2018). However, ~~In~~ in this study, relative humidity was exceptionally high with the mean value of 71±26%. It showed strong

Formatted: Font: (Default) Times New Roman, 小四, Font color: Text 1, Pattern: Clear

Formatted: Font: (Default) Times New Roman, 小四, Font color: Auto, Pattern: Clear

diurnal variation, reaching ~~with~~ its minimum in the daytime and even close to 100% in the nighttime (Figure 1~~2~~a). Additionally~~Also~~, wind speed was low of 0.54±0.59m/s with a maximum of 2.6m/s. ~~Due to t~~This stagnant synoptic condition led to elevated~~,~~ ~~the mean~~ concentrations of main gaseous pollutants such as O_3, SO_2, and NO_2, ~~reached~~ with mean values of 86.0±47.8μg/m^3, 11.8±3.4μg/m^3, and 63.3±27.9μg/m^3, respectively, even higher than those during the non-dust period.

We further divided the dust event into three stages based on the temporal characteristics of PM_{10} and the transport patterns of air masses ~~transport patterns~~. As shown in ~~Figure 2d~~Figure 1d, PM_{10} quickly climbed from 4:00 on October 29 and reached a maximum of 436μg/m^3 after 8 hours. The air masses primarily ~~mainly~~ originated from the semi-arid regions of northwest China (~~Figure 3d~~Figure 2d), ~~and this~~which was consistent with both the near surface wind observation (~~Figure 2a~~Figure 1a) and wind lidar observation (~~Figure 3a~~Figure 2a). The wind profiles showed prevailing ~~dominant~~ northwest winds from the surface up to ~~ground to the altitudes of~~ around 2km before ~~the~~ noon ~~of~~ on October 29, indicating the presence of a strong synoptic system. Afterwards, PM_{10} quickly decreased to 199 μg/m^3 at 20:00, October 29 within 8 hours. This was primarily attributed~~mainly due~~ to the shift of wind directions. As shown in ~~Figure 3a~~Figure 2a, while ~~although the~~ winds ~~at altitudes of higher than~~above 700m continued to blow~~kept blowing~~ from the northwest, ~~the~~ near-surface winds had shifted ~~turned~~ from the southeast. Due to~~As~~ Shanghai's ~~is a~~ coastal ~~city and~~location adjacent to the East China Sea, the relatively clean southeasterlies diluted the local air pollutants, thereby explaining~~and thus explained~~ the quick decline ~~decrease of~~ in PM10 concentrations. This initial ~~short~~ dust episode occurring from 4:00 - 13:00~~,~~ ~~—~~ on October 29 was defined as Stage P1.

Formatted: Font: (Default) Times New Roman, 小四, Font color: Auto, Pattern: Clear

Formatted: Font: (Default) Times New Roman, 小四, Font color: Auto, Pattern: Clear

Formatted: Font: (Default) Times New Roman, 小四, Font color: Auto, Pattern: Clear

Formatted: Font: (Default) Times New Roman, 小四, Font color: Auto, Pattern: Clear

Formatted: Font: (Default) Times New Roman, 小四, Font color: Auto, Pattern: Clear

Formatted: Font: (Default) Times New Roman, 小四, Font color: Auto, Pattern: Clear

Formatted: Font: (Default) Times New Roman, 小四, Font color: Auto, Pattern: Clear

Formatted: Font: (Default) Times New Roman, 小四, Font color: Auto, Pattern: Clear

Formatted: Font: (Default) Times New Roman, 小四, Font color: Auto, Pattern: Clear

Formatted: Font: (Default) Times New Roman, 小四, Font color: Auto, Pattern: Clear

Formatted: Font: (Default) Times New Roman, 小四, Font color: Auto, Pattern: Clear

Formatted: Not Superscript/ Subscript

Formatted: Font: (Default) Times New Roman, 小四, Font color: Auto, Pattern: Clear

Formatted: Font: (Default) Times New Roman, 小四, Font color: Auto, Pattern: Clear

Despite the persistent~~However, the prevailing~~ southeasterly winds, the dust event did not come to a complete halt.~~didn't fully terminate the dust event.~~ Even under these prevailing winds~~the persistent southeasterlies~~, hourly PM_{10} concentrations remained ~~stayed~~ above 150 μg/m^3 until November 1, gradually decreasing ~~and then decreased~~ to 65 μg/m^3 at 03:00, November 1 (Figure ~~2d~~1d). Compared to P1, wind speed during this stage was as low as 0.4 ± 0.5m/s, while RH was moderately high of 70 ± 26%. Although the daytime RH stayed low between 30% and 50%, it frequently soared above~~reached over~~ 90% at nighttime. ~~Figure 3e~~ Figure 2e shows that although the air masses originated from the Gobi Desert, they also traversed ~~passed over~~ considerable coastal regions. The wind profiles further indicated that while~~also showed that although~~ northwest winds prevailed at altitudes higher than 500m, ~~the~~ east and northeast winds were dominant below 500m (Figure ~~3b~~2b). Consequently, ~~This explained~~ the relatively high ~~relative humidity~~RH during this period can be attributed to~~due to~~ the mixing ~~between~~ of dust plumes ~~and~~ with coastal sea breezes. This dust episode from 14:00, October 29 to 3:00~~,~~ on November 1 was designated ~~defined~~ as Stage P2.

Following ~~After~~ P2, PM_{10} and $PM_{2.5}$ rose again and peaked at 5:00 and 9:00~~,~~ on November 2 with the hourly concentration of 199 and 117μg/m^3, respectively. Different from P1 and P2, the air masses during this stage originated from the Shandong Peninsula and the northern region of Jiangsu province, and then migrated over the Yellow Sea and the East China Sea (~~Figure 3f~~Figure 2f). Typically~~Usually~~, ~~the~~ dust plumes tend to travel eastward, ~~would transport further eastwards and~~ impacting the western Pacific region and even distant ~~faraway~~ oceanic regions (Wang et al., 2018; Nagashima et al., 2016). However, in this case, the air masses evidently deviated ~~deflected~~ and pushed the dust back towards ~~to~~ the mainland. The wind profiles on

Formatted: Font: (Default) Times New Roman, 小四, Font color: Text 1, Pattern: Clear
Formatted: Font: (Default) Times New Roman, 小四, Font color: Text 1, Pattern: Clear
Formatted: Font: (Default) Times New Roman, 小四, Font color: Text 1, Pattern: Clear
Formatted: Font: (Default) Times New Roman, 小四, Font color: Text 1, Pattern: Clear
Formatted: Font: (Default) Times New Roman, 小四, Font color: Text 1, Pattern: Clear
Formatted: Font: (Default) Times New Roman, 小四, Font color: Text 1, Pattern: Clear
Formatted: Font: (Default) Times New Roman, 小四, Font color: Text 1, Pattern: Clear
Formatted: Font: (Default) Times New Roman, 小四, Font color: Text 1, Pattern: Clear
Formatted: Font: (Default) Times New Roman, 小四, Font color: Text 1, Pattern: Clear
Formatted: Font: (Default) Times New Roman, 小四, Font color: Text 1, Pattern: Clear
Formatted: Font color: Text 1
Formatted: Font: (Default) Times New Roman, 小四, Font color: Text 1, Pattern: Clear
Formatted: Font color: Text 1
Formatted: Font: (Default) Times New Roman, 小四, Font color: Text 1, Pattern: Clear
Formatted: Font: (Default) Times New Roman, 小四, Font color: Text 1, Pattern: Clear
Formatted: Font: (Default) Times New Roman, 小四, Font color: Text 1, Pattern: Clear
Formatted: Font color: Text 1
Formatted: Font: (Default) Times New Roman, 小四, Font color: Text 1, Pattern: Clear
Formatted: Font color: Text 1
Formatted: Font: (Default) Times New Roman, 小四, Font color: Text 1, Pattern: Clear
Formatted: Font: (Default) Times New Roman, 小四, Font color: Text 1, Pattern: Clear

November 2 revealed that~~also showed~~ winds within ~~at~~ the detected altitude range ~~of altitudes~~, predominantly originated ~~all came~~ from the eastern and southeastern oceanic regions (~~Figure 3c~~Figure 2c). This probably indicated the mixing between dust plumes and humid oceanic air masses was quite sufficient, which was also reflected by the highest average RH of 76 ± 24% among the three stages of the dust event. Moreover~~In addition~~, the concentrations of O_3 and NO_2 at this stage were higher than those of P1 and P2, potentially promoting~~which could be conducive to~~ the formation of secondary aerosol components and will be discussed later. This rarely observed dust backflow transport episode from 4:00~~,~~ on November 1 to 23:00~~,~~ on November 2 was designated ~~defined~~ as Stage P3.

Formatted: Font: (Default) Times New Roman, 小四, Font color: Text 1, Pattern: Clear

Formatted: Font: (Default) Times New Roman, 小四, Font color: Text 1, Pattern: Clear

Formatted: Font: (Default) Times New Roman, 小四, Font color: Text 1, Pattern: Clear

Formatted: Font: (Default) Times New Roman, 小四, Font color: Text 1, Pattern: Clear

Formatted: Font: (Default) Times New Roman, 小四, Font color: Text 1, Pattern: Clear

Formatted: Font: (Default) Times New Roman, 小四, Font color: Auto, Pattern: Clear

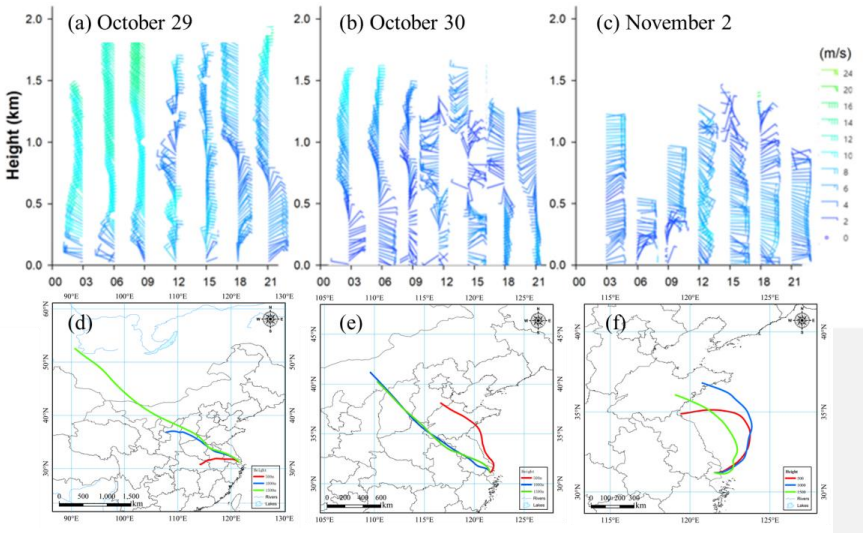

Figure ~~3~~2. Wind profiles observed by a wind profiler radar on (a) October 29, (b) October 30, and (c) November 2. 48-hour backward trajectories simulated at the sampling site starting from (d) 4:00 AM, October 29, (e) 9:00 AM, October 30, and (f) 13:00 PM, November 2. The red, blue, and green trajectories represented starting altitudes of 100, 500, and 1500m, respectively.

3.2. Comparisons of aerosol chemical compositions among the three dust stages

Figure 34a shows the time-series of hourly aerosol chemical components, including SNA (NO_3^-, SO_4^{2-}, and NH_4^+), OM ~~(organic matters = 2*OC)~~, EC, and mineral aerosols ~~([Minerals]= (2.2*Al+2.49*Si+1.63*Ca+2.42*Fe+1.94*Ti), (Malm et al., 1994))~~ in $PM_{2.5}$. During P1, the mean concentration of SNA was 49.9 ± 31.6 μg/m^3. The mineral aerosols reached 16.4 ± 14.6 μg/m^3, accounting for 19% in $PM_{2.5}$. The contribution of OM to $PM_{2.5}$ was almost identical to that of mineral aerosols (Figure ~~4b~~3b).

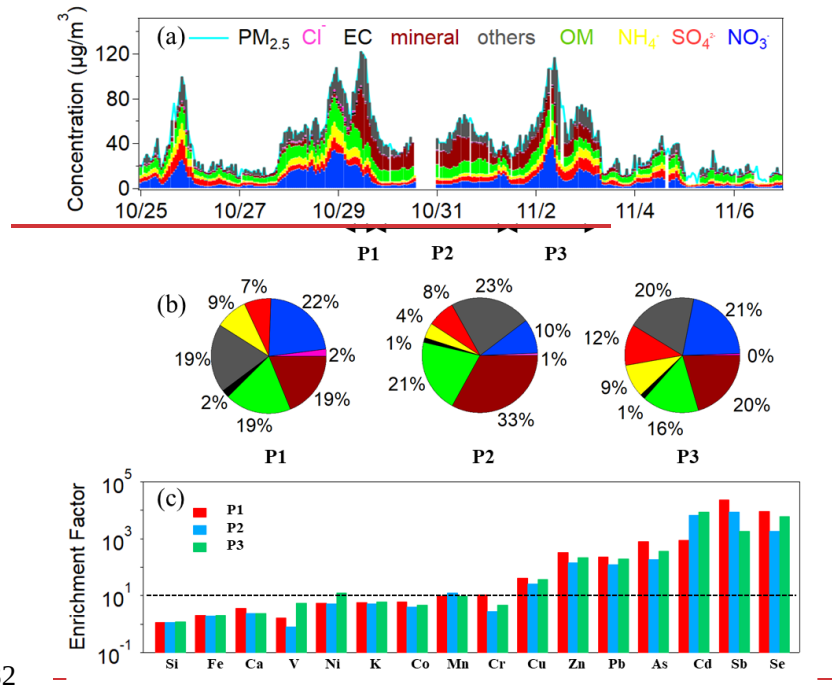

382

383

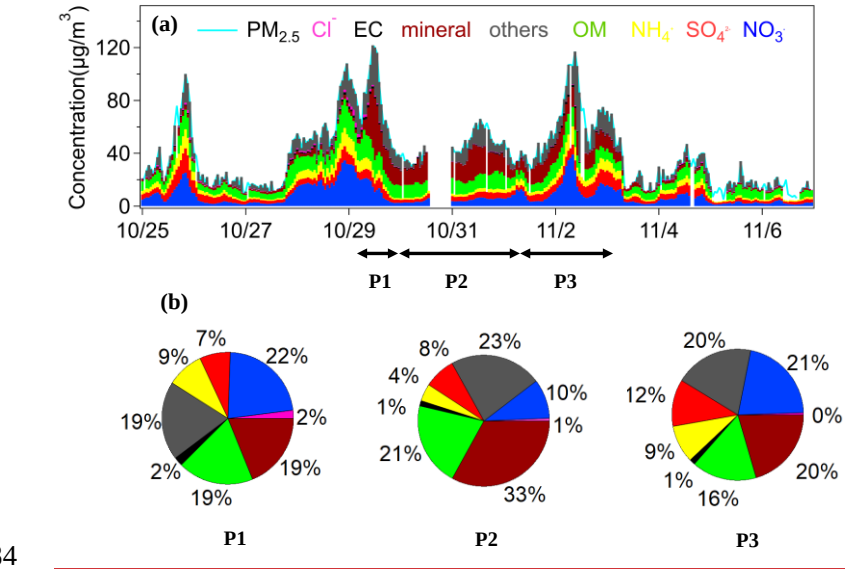

384

385 Figure 43. (a) Times-series of major chemical components in $PM_{2.5}$ during the study

period. (b) The mean proportion of major chemical components in $PM_{2.5}$ during the three dust stages. ~~(c) Enrichment factors of elements in $PM_{2.5}$ during the three dust stages.~~

During P2, mineral aerosols increased to 23.4±54.1μg/m^3 and accounted for 33% in $PM_{2.5}$, representing the highest among all three stages (~~Figure 4b~~Figure 3b). Due to the continuous dilution effect of dust on local anthropogenic pollutants, the concentrations and proportions of SNA in $PM_{2.5}$ were the lowest during this stage. For instance, NO_3^- only accounted for 10% in $PM_{2.5}$, indicating a suppression of ~~the~~ nitrate formation ~~of nitrate was suppressed~~ to ~~a certain~~some extent. The levels of OM didn't exhibit ~~show~~ obvious changes and averaged 10.1±2.1μg/m^3, accounting for 21% in $PM_{2.5}$.

During P3, mineral aerosols averaged 11.9±2.7μg/m^3, ranking the lowest among all three stages. The proportion of mineral aerosols in $PM_{2.5}$ decreased to 20%, suggesting the dust backflow from the ocean was less enriched in mineral components. Compared to P2, SNA showed significant increases and much stronger diurnal variations during P3. SO_4^{2-}, NO_3^-, and NH_4^+ averaged 6.7 ± 2.4, 12.4 ± 8.9, and 5.4 ± 2.7μg/m^3, respectively. As shown in ~~Figure 4b~~Figure 3b, the contribution of nitrate to $PM_{2.5}$ increased to 21%, while that of sulfate rose to 12%, the highest among all three stages. The concentration of OM (9.3±3.2μg/m^3) and its proportion (16%) ~~of OM~~ during P3 were lower than the other two stages, likely ~~which was probably~~ due to the unconventional ~~unusual~~ dust backflow transport pathway.

~~Enrichment factors (EFs) of the measured elements in $PM_{2.5}$ were calculated by using Al as a reference element, i.e., $EF_x=(X/Al)_{aerosol}/(X/Al)_{crust}$, where X was the element of interest. As shown in Figure 4c, elements such as Si, Fe, and Ca were less~~

Formatted: Font: (Default) Times New Roman, 小四, Font color: Text 1, Pattern: Clear

Formatted: Font: (Default) Times New Roman, 小四, Font color: Text 1, Pattern: Clear

Formatted: Font: (Default) Times New Roman, 小四, Font color: Text 1, Pattern: Clear

Formatted: Font: (Default) Times New Roman, 小四, Font color: Auto, Pattern: Clear

Formatted: Font: (Default) Times New Roman, 小四, Font color: Auto, Pattern: Clear

~~enriched as they mainly derived from the crust. While for anthropogenic elements including Cu, Zn, Pb, As, Cd, Sb, and Se, they were enriched by different extents with EFs between 10 and 10,000. In addition, these elements above were more enriched during P1 than P2 and P3. The dust transport pathway via inland areas during P1 should be the main cause as anthropogenic sources such as metallurgical industries, coal-fired plants, and smelters were widely located in inland regions. Exceptions were found for Ni and V, which were often used as tracers for heavy oil combustion. EFs of Ni and V exhibited higher values during P3 than P1 and P2. Since the dust backflow transport pathway during P3 had almost two days travelling durations over the East China Sea, which was on the one of the busiest international shipping trade routes (Fan et al., 2016), the enrichments of Ni and Vi were probably ascribed to the mixing between dust and marine shipping emissions.~~

3.3. Unconventional features of the dust episodes

3.3.1. ~~Effect of u~~Unusually enhanced~~high~~ O_3 ~~on the formation of secondary aerosols~~ during ~~P2~~dust

Figure ~~5~~ 4 shows the hourly near surface ozone concentrations and vertical profiles of ozone during the study period. Interestingly, a few high O_3 peaks occurred during the dust event (Figure ~~4~~5a). O_3 averaged 92.8 ± 52.8μg/m^3 during the dust, about 50% higher than the non-dust days. Among the three dust stages, O_3 substantially increased from 35.9 ± 36.4μg/m^3 during P1 to 80.7 ± 41.2μg/m^3 during P2, and further rose to 104.0 ± 48.7μg/m^3 during P3. The low O_3 during P1 can be attributed~~was due~~ to the cleansing effect of the strong dust associated with the ~~strong~~ cold front, which was consistent with~~as similar as~~ previous studies that reported

Formatted: Font: 小四, Bold

Formatted: Font: (Default) Times New Roman, 小四, Font color: Auto, Pattern: Clear

Formatted: Font: (Default) Times New Roman, 小四, Font color: Auto, Pattern: Clear

Formatted: Font: (Default) Times New Roman, 小四, Font color: Auto, Pattern: Clear

reduced ~~low~~ oxidant~~s~~ concentrations ~~were usually observed~~ during intense ~~strong~~ dust events (Benas et al., 2013). Regarding ~~As for~~ the relatively high O_3 during P2 and P3, several causes may contribute to this phenomenon~~be responsible~~. Firstly, the mean wind speed was low of 0.4 and 0.6 m/s during P2 and P3, respectively. Consequently~~Thus~~, this weak synoptic system exerted a weak dilution effect on the local air pollutants. A numerical study conducted during a similar period suggested that the reduction of boundary layer height and the warming of the lower atmosphere accelerated the ozone formation by ~1 ppbv/h (Wang et al., 2020). Secondly, since the dust plume travelled mostly over the coastal and oceanic areas, a portion ~~part~~ of O_3 could be transported from the high ozone oceanic areas (Wang et al., 2022b). Thirdly, the ozone lidar also detected ~~observed~~ high O_3 stripes during P2 and P3. As shown in Figure 5b, the high O_3 profiles extended from the surface to around 1km and the profile structure was similar to that of aerosol depolarization ratio. The subsidence of dust particles likely contributed to downward transport of~~probably down drafted~~ high-altitude O_3, thereby influencing ~~and also contributed to~~ the elevated ~~high~~ O_3 near the ground (Yang et al., 2022).

Formatted: Font: (Default) Times New Roman, 小四, Font color: Auto, Pattern: Clear

Formatted: Font: (Default) Times New Roman, 小四, Font color: Auto, Pattern: Clear

Formatted: Font: (Default) Times New Roman, 小四, Font color: Auto, Pattern: Clear

Formatted: Font: (Default) Times New Roman, 小四, Font color: Auto, Pattern: Clear

Formatted: Font: (Default) Times New Roman, 小四, Font color: Auto, Pattern: Clear

Formatted: Font: (Default) Times New Roman, 小四

Formatted: Font: (Asian) 宋体, 小四

Formatted: Font: (Default) Times New Roman, 小四

Formatted: Font: (Default) Times New Roman, 小四, Font color: Auto, Pattern: Clear

Formatted: Font color: Auto

Formatted: Font: (Default) Times New Roman, 小四, Font color: Auto, Pattern: Clear

Formatted: Font color: Auto

Formatted: Font: (Default) Times New Roman, 小四, Font color: Auto, Pattern: Clear

Formatted: Font: (Default) Times New Roman, 小四, Font color: Auto, Pattern: Clear

Formatted: Font color: Auto

Formatted: Font: (Default) Times New Roman, 小四, Font color: Auto, Pattern: Clear

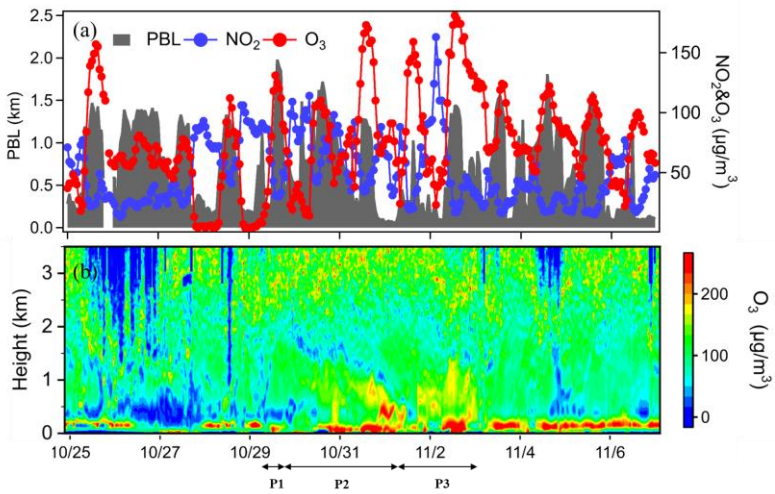

Figure ~~5~~4. (a) Time-series of near surface O_3, NO_2 and planetary boundary layer height (b) Vertical profiles of ozone observed by the ozone Lidar.

~~To investigate the effect of the relatively high O_3 on the formation of secondary aerosols, Figure 6 displays the relationship between sulfate/nitrate and ammonium. The strong correlations of sulfate-ammonium (R^2=0.91) and nitrate-ammonium (R^2 = 0.93) were expected. The scatters were further color-coded by O_3 and it could be seen that higher sulfate, nitrate, and ammonium tended to be formed under higher O_3 concentrations, suggesting the potential role of photochemistry in promoting the formation of secondary aerosols.~~

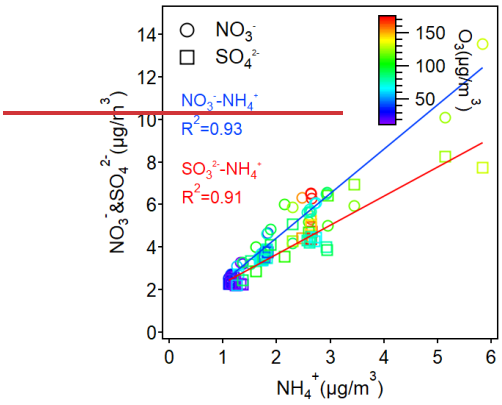

~~Figure 6. Linear relationship between sulfate/nitrate and ammonium with scatters colored by the concentrations of O_3 during P2~~

~~Figure 7 displays the linear relationship between sulfate and PM_{10}, ALWC, O_3, and HONO, respectively. Obviously, sulfate had no correlation with PM_{10} (Figure 7a), indicating that dust contributed negligibly to sulfate. Also, sulfate had almost no or even a weakly negative correlation with ALWC (Figure 7b), suggesting aqueous-phase processing was not a major reaction pathway of secondary aerosols during P2. In contrast, we found that sulfate correlated positively with O_3 (R^2=0.38, Figure 7c) and negatively correlated with HONO (R^2=0.25, Figure 7d). It was well recognized that HONO was an important precursor to OH radical and it was estimated that HONO accounted for 30%~60% of the OH budget in Shanghai (Bernard et al., 2016). The moderate correlations between sulfate and O_3/HONO corroborated the discussion above that the formation of secondary aerosols during P2 should be mainly promoted via the gas-phase oxidations.~~

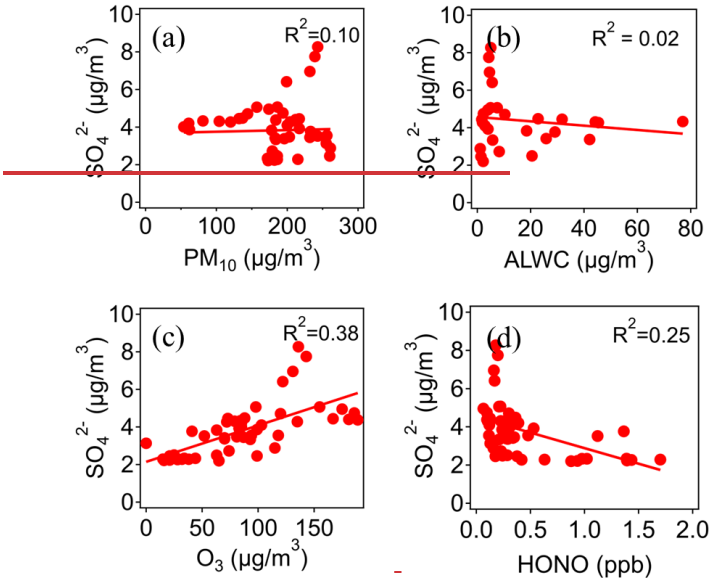

Figure 7. Linear relationship between sulfate and (a) PM_{10}, (b) ALWC, (c) O_3, and (d) HONO during P2

As similar as sulfate, nitrate didn't show correlation with ALWC (Figure 8b) but moderately correlated with O_3 (R^2=0.43, Figure 8c). Figure 8a displays the temporal variation of NO_2, O_3, HONO, and NO_3^- during P2. It can be found that although NO_2 was high at night as well as for HONO, the concentrations of NO_3^- were relatively low, indicating a low formation potential of secondary aerosols. Figure 2a shows that RH during P2 was relatively low at nighttime with a minimum of 31%, suggesting the aqueous reactions could be suppressed to some extents. During the daytime, O_3 reached its maximum while HONO reached its minimum, both contributing to the high levels of oxidants. The co-variation of nitrate and sulfate with O_3 (Figure 8a) confirmed that although dust often suppressed the formation of atmospheric oxidants, the photochemistry reactions under unusually high O_3 concentrations dominated the

~~formation of sulfate and nitrate during P2 in this study.~~

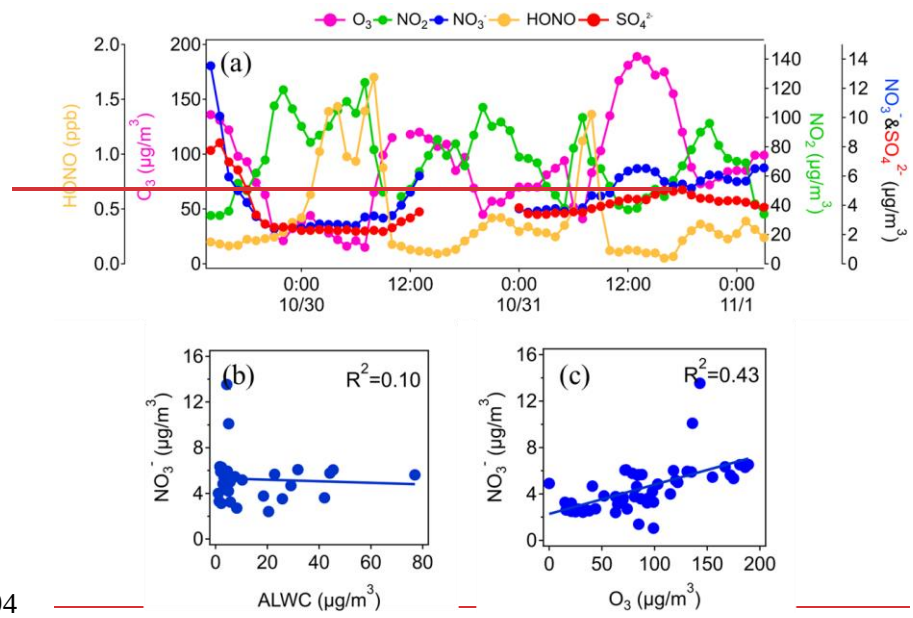

~~Figure 8. (a) Temporal variations of O_3, NO_2, HONO, nitrate, and sulfate during P2. Linear relationship between nitrate and (b) ALWC and (c) O_3.~~

~~3.4. Aerosol chemistry under dust backflows during P3~~

~~3.4.1. Evidence of d~~3.3.2. Dust backflows during P3

The dust during P3 was diagnosed as a backflow transport pathway from the mainland to Shanghai through the Yellow Sea and the East China Sea, as determined by~~according to~~ the backward trajectory analysis (~~Figure 3f~~Figure 2f). This unconventional ~~atypical~~ dust transport route, termed ~~pathway observed in this study was defined as the~~ "dust backflow", was consistent with a similar occurrence~~,~~ in 2014 when dust from northern China detoured over Shanghai (Wang et al., 2018). In this section, we have provided further ~~more~~ evidences of the dust backflow from various aspects.

Formatted: Font: (Default) Times New Roman, 小四, Font color: Auto, Pattern: Clear

Formatted: Font: (Default) Times New Roman, 小四, Font color: Auto, Pattern: Clear

Formatted: Font: (Default) Times New Roman, 小四, Font color: Auto, Pattern: Clear

Formatted: Font: (Default) Times New Roman, 小四, Font color: Auto, Pattern: Clear

Field Code Changed

Formatted: Not Highlight

Formatted: Font: (Default) Times New Roman, 小四, Font color: Auto, Pattern: Clear

~~Figure 3f~~Figure 2f illustrates that ~~shows~~ the dust drifted away from the Shandong Peninsula, thus we selected two coastal sites in Shandong province for supplementary analysis. ~~Figure 9~~ Figure S2 compares the time-series of hourly air pollutants at Qingdao, Lianyungang, and Shanghai. At Qingdao and Lianyungang, high PM_{10} concentrations were observed during October 30 – 31, indicating the invasion of dust in these regions. After about two days, PM_{10} ~~showed a~~ peaked in Shanghai ~~at~~ on early November 2 ~~at Shanghai~~. This temporal consistency aligned ~~This was consistent~~ with the simulation duration of the backward trajectories, which lasted ~~i.e.,~~ around 48 hours (Figure ~~23~~f). In Figure 9, it can be observed~~could be seen~~ that in the upstream dust ~~upstream~~ regions (i.e., Qingdao and Lianyungang), PM_{10} varied negatively with NO_2 and CO (the highlighted period in the figure). While in Shanghai, positive correlations between PM_{10} and both NO_2 (R^2=0.32) ~~as well as between PM_{10}~~ and CO (R^2=0.55) indicated that the dust during P3 served ~~had acted~~ as a carrier ~~of the~~for gaseous pollutants ~~rather than acting~~but not a diluter.

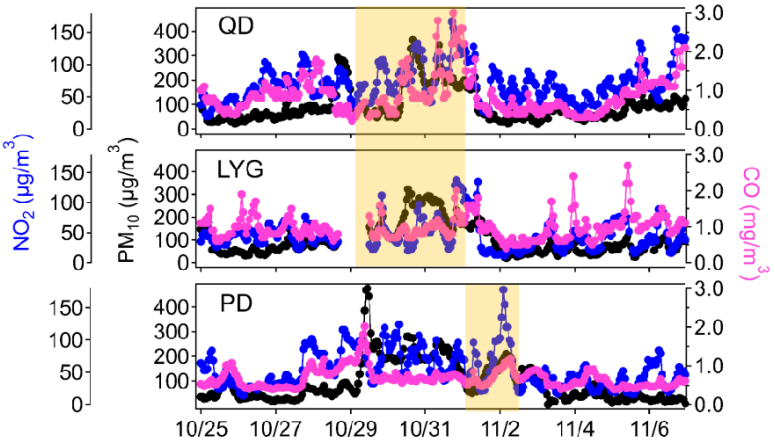

~~Figure 9. Time-series of PM_{10}, NO_2, and CO at Qingdao, Lianyungang, and Pudong.~~

Formatted: Font: (Default) Times New Roman, 小四, Font color: Auto, Pattern: Clear

Formatted: Font: (Default) Times New Roman, 小四, Font color: Auto, Pattern: Clear

Formatted: Font: (Default) Times New Roman, 小四, Font color: Auto, Pattern: Clear

Formatted: Font: (Default) Times New Roman, 小四, Font color: Auto, Pattern: Clear

Formatted: Font: (Default) Times New Roman, 小四, Font color: Auto, Pattern: Clear

Formatted: Font: (Default) Times New Roman, 小四, Font color: Auto, Pattern: Clear

~~The dust periods at these three sites are highlighted.~~

~~More evidence of dust backflows was provided from the perspective of aerosol chemical tracers. As discussed in Section 3.2, enrichment factors of V and Ni were the highest during P3. Figure 10a further displays the time series of V and Ni and they varied significantly during the study period. The mass concentrations of V and Ni increased 4 and 1.8 times during P3 compared to P2, respectively. This indicated that the dust had mixed with pollutants from marine vessel emissions and transported back to Shanghai.~~

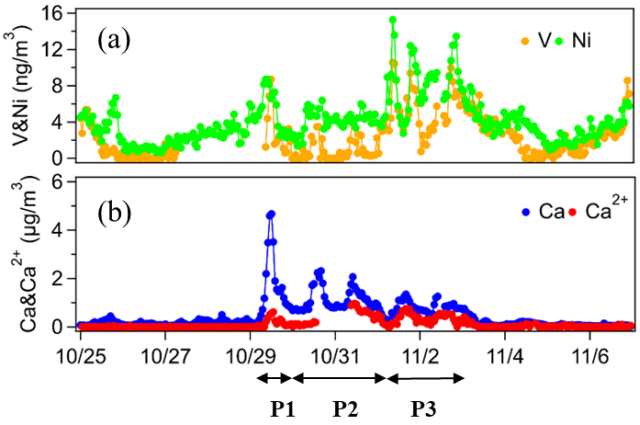

~~Figure 10. Time series of (a) V, Ni, (b) Ca, and Ca^{2+} during the study period~~

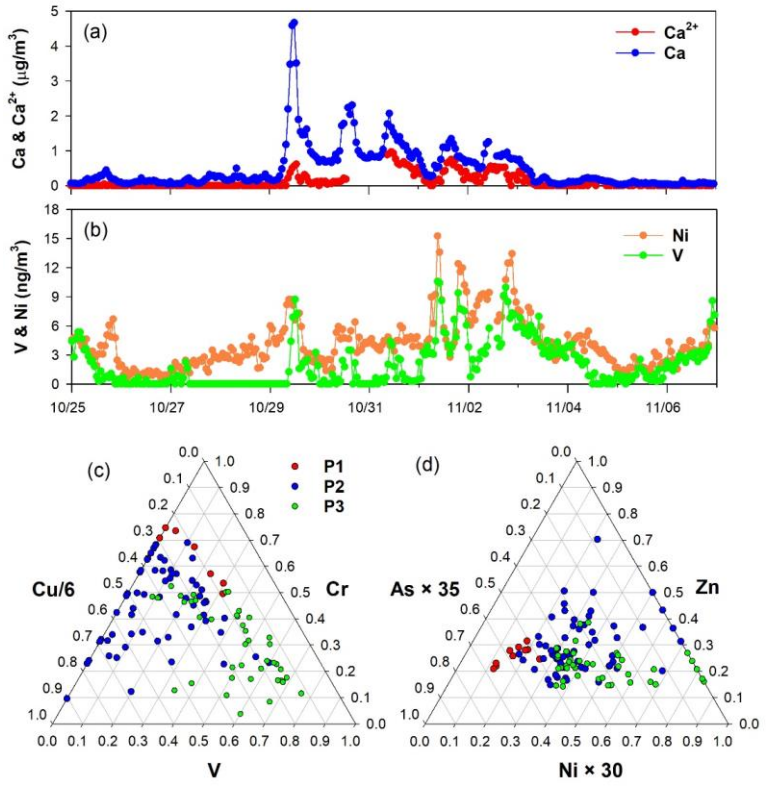

Figure 5. Time-series of (a) Ca, Ca^{2+}, (b) V, and Ni during the study period. (c) Cu-Cr-V ternary diagram and (d) As-Zn-Ni ternary diagram among the P1 – P3 dust episodes. Due to substantial concentration differences of various elements, some elements are artificially changed to make most scatters appear around the centroid.

Formatted: Caption, Centered, Space Before: 9.5 pt, After: 9.5 pt

Additional ~~More~~ evidence of dust backflows was provided from the perspective of aerosol chemical tracers. ~~Figure 10b~~ Figure 5a plots the time-series of Ca and Ca^{2+}, ~~which~~ represent~~ed~~ the total calcium and the soluble part of calcium, respectively. It was observed that Ca and Ca^{2+} didn't exhibit ~~quite~~ a proportional variation trend, which

Formatted: Font: (Default) Times New Roman, 小四, Font color: Auto, Pattern: Clear

should be related to the solubility of calcium during different dust stages. During P1, the mean concentration of Ca reached the highest of 1.63 ± 1.53μg/m^3 while Ca^{2+} was the lowest of 0.21 ± 0.20μg/m^3, thus resulting in the lowest Ca^{2+}/Ca ratio of 0.10 ± 0.08. As discussed in Section 3.1, dust during P1 was the strongest and thus it contained higher fractions of minerals, primarily ~~which were mainly~~ in the form of insoluble metal oxides. ~~–~~ The average concentrations of Ca^{2+} and Ca during P2 were 0.33 ± 0.28μg/m^3 and 1.11 ± 0.46μg/m^3, respectively, resulting in~~with~~ the higher Ca^{2+}/Ca ratio of 0.27 ± 0.20. As a comparison, the average concentrations of $Ca^{2+}$and Ca during P3 reached 0.34 ± 0.20μg/m^3 and 0.78 ± 0.27μg/m^3, respectively, yielding the highest Ca^{2+}/Ca ratio of 0.38 ± 0.19. The significantly ~~much~~ higher solubility of calcium during P3 should be directly related to the prolonged presence ~~lingerer~~ of dust plumes over the open ocean. The abundant water vapor over the ocean could accelerate the dissolution of the insoluble components in particles during the mixing between continental dust and oceanic air masses. Additionally, the backflow transport pathway facilitated the entrainment of sea salts and contributed to the increase of soluble calcium.

~~As discussed in Section 3.2, enrichment factors of V and Ni were the highest during P3.~~ Figure ~~10a~~5b provides additional insights by displaying ~~further displays~~ the time-series of V and Ni, which are typical tracers of oil combustions (Becagli et al., 2012). ~~and t~~They varied significantly during the study period, ~~-~~ and ~~T~~the mass concentrations of V and Ni increased 4 and 1.8 times during P3 compared to P2, respectively. ~~This indicated that the dust had mixed with pollutants from marine vessel emissions and transported back to Shanghai.~~ Consistently, the enrichment factors of Ni and V displayed higher values during P3 than P1 and P2 (Figure S3). The trends are substantiated in the ternary diagrams, which are commonly applied to illustrate the

Formatted: Font: (Default) Times New Roman, 小四, Font color: Auto, Pattern: Clear

Formatted: Font: (Default) Times New Roman, 小四, Font color: Auto, Pattern: Clear

Formatted: Not Superscript/ Subscript

Formatted: Font: (Default) Times New Roman, 小四, Font color: Auto, Pattern: Clear

Formatted: Font: (Default) Times New Roman, 小四, Font color: Auto, Pattern: Clear

Formatted: Font: (Default) Times New Roman, 小四, Font color: Auto, Pattern: Clear

Formatted: Font: (Default) Times New Roman, 小四, Font color: Auto, Pattern: Clear

Formatted: Font: (Default) Times New Roman, 小四, Font color: Auto, Pattern: Clear

Formatted: Font: 小四

Formatted: Font: 小四

Formatted: Font: (Default) Times New Roman, 小四, Font color: Auto, Pattern: Clear

Formatted: Font: (Default) Times New Roman, 小四, Font color: Auto, Pattern: Clear

Formatted: Font: (Default) Times New Roman, 小四, Font color: Auto, Pattern: Clear

Formatted: Font: (Default) Times New Roman, 小四, Font color: Auto, Pattern: Clear

relative abundances of three components and infer the source variations (Bozlaker et al., 2019; Cwiertny et al., 2008; Laskin et al., 2005). As shown in the Cu-Cr-V ternary diagram (Fig. 5c), the dust samples during P1 were positioned away from the V-apex. As a comparison, the dust samples during P2 exhibited greater scattering, manifesting enhanced anthropogenic contributions, e.g., from chrome plating industries (Hammond et al., 2008). Compared to P2, the dust samples during P3 moved toward the V-apex, indicating a higher contribution from oil combustions (Becagli et al., 2012). A similar pattern was observed in the As-Zn-Ni ternary diagram (Fig. 5d). The majority of dust samples during P2 spanned across the diagram, reflecting contributions from mixed anthropogenic sources. Reciprocally, P3 was closer to the Ni-apex. These lines of evidences collectively confirmed that the dust had mixed with pollutants from marine vessel emissions over one of the busiest international shipping trade routes (Fan et al., 2016) and was subsequently transported back to Shanghai.

3.4. Formation of secondary aerosols during the dust long-range transport

3.4.1. Comparison of typical chemical tracers

Formatted: Font: (Default) Times New Roman, 小四, Font color: Auto, Pattern: Clear

Formatted: Font: 小四

Formatted: Font: (Default) Times New Roman, 小四, Font color: Auto, Pattern: Clear

Formatted: Font: 小四

Formatted: Font: 小四

Formatted: Font: (Default) Times New Roman, 小四, Font color: Auto, Pattern: Clear

Formatted: Font: 小四

Formatted: Font: (Default) Times New Roman, 小四, Font color: Auto, Pattern: Clear

Formatted: Font: (Default) Times New Roman, 小四, Font color: Auto, Pattern: Clear

Formatted: Font: (Default) Times New Roman, 小四, Font color: Auto, Pattern: Clear

Formatted: Font: (Default) Times New Roman, 小四, Font color: Auto, Pattern: Clear

Formatted: Font: (Default) Times New Roman, 小四, Font color: Auto, Pattern: Clear

Formatted: Font: Bold

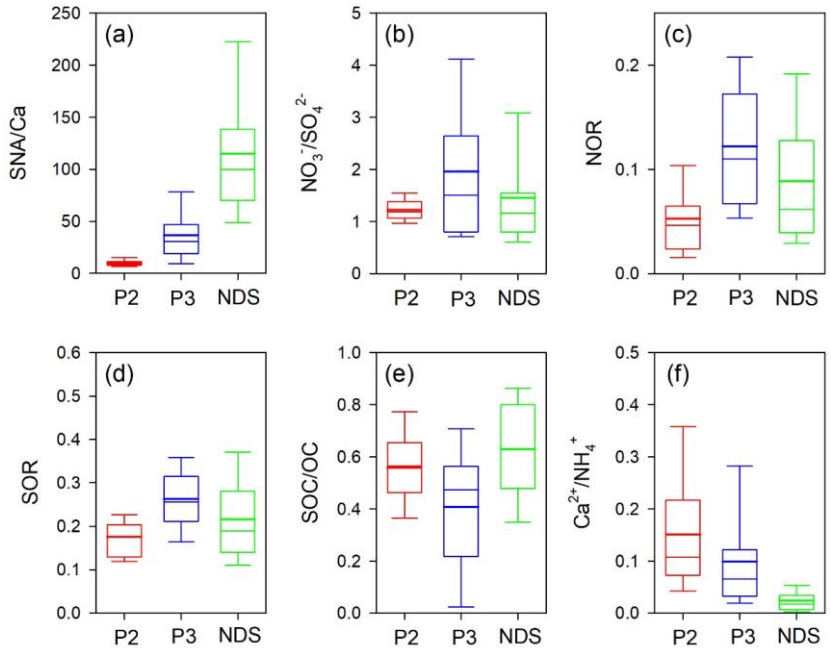

Figure 6. Box plots of (a) SNA/Ca, (b) NO_3^-/SO_4^{2-}, (c) NOR, (d) SOR, (e) SOC/OC, and (f) Ca^{2+}/NH_4^+ during P2, P3, and NDS, respectively.

To delve deeper into the formation characteristics of secondary aerosols in different stages, a variety of chemical tracers was investigated. The P1 dust stage was excluded from statistical analysis due to its short duration and limited data availability. Fig. 6a shows the comparison of SNA/Ca ratios during P2, P3 and non-dust days (NDS). The SNA/Ca ratio can be used to assess the relative changes between secondary production and primary dust emission by eliminating the impact of meteorological conditions among different periods (Zheng et al., 2015). Compared to the two dust episodes, the SNA/Ca ratio is significantly higher during NDS. This can be attributed to the much lower concentrations of mineral aerosols during NDS, thus resulting in the

Formatted: Font: Not Bold
Formatted: Not Highlight
Formatted: Font: (Default) Times New Roman, 小四, Font color: Auto, Pattern: Clear
Formatted: Font: Not Bold
Formatted: Font: (Default) Times New Roman, 小四, Font color: Auto, Pattern: Clear
Formatted: Font: Not Bold
Formatted: Font: Not Bold
Formatted: Font: Not Bold
Formatted: Not Highlight
Formatted: Font: Not Bold
Formatted: Font: Not Bold
Formatted: Font: (Default) Times New Roman, 小四, Font color: Auto, Pattern: Clear
Formatted: Font: Not Bold
Formatted: Font: Not Bold
Formatted: Font: Not Bold
Formatted: Font: (Default) Times New Roman, 小四, Font color: Auto, Pattern: Clear
Formatted: Font: (Default) Times New Roman, 小四, Font color: Auto, Pattern: Clear
Formatted: Font: Not Bold
Formatted: Font: Not Bold
Formatted: Font: Not Bold
Formatted: Font: (Default) Times New Roman, 小四, Font color: Auto, Pattern: Clear
Formatted: Font: Not Bold

higher SNA relative to Ca. In terms of comparing P2 and P3, the average SNA/Ca ratio during P3 was 3 times that of P2, indicating that the formation of secondary inorganic aerosols was more prominent during the dust backflow. Regarding the NO_3^-/SO_4^{2-} ratios (Fig. 6b), they were close between NDS and P2, with NO_3^- slightly exceeding SO_4^{2-}. The range of NO_3^-/SO_4^{2-} was the largest during P3 with a mean value of around 2, suggesting that the dust backflow was more conducive to the accumulation of nitrate. The nitrogen oxidation ratio (NOR = $NO_3^-/(NO_3^- + NO_2)$) and the sulfur oxidation ratio (SOR = $SO_4^{2-}/(SO_4^{2-} + SO_2)$) were further used to gauge the extent of nitrate and sulfate formation, both showing trends of P3>NDS>P2 (Fig. 6c & 6d). It should be noted that NOR and SOR cannot be used to realistically characterize the extent of nitrogen and sulfur oxidation during transport-dominated pollution cases, as upstream aging aerosols can significantly increase the above ratios (Ji et al., 2018). In the following discussion, we will focus on the formation mechanism of SNA during different dust stages.

The results of SOC/OC ratios differed from the above analysis that SOC/OC was lower during P3 than during P2 and NDS (Fig. 6e), suggesting that the formation of secondary organic aerosols was not favored via the dust backflow. This may be due to its maritime transport pathway as the emission intensity of volatile organic compounds from the ocean is much lower than that from land sources . Consequently, the lacking of organic aerosol precursors could be the main cause for the lower SOC/OC ratios during P3. Finally, the Ca^{2+}/NH_4^+ ratio was employed to assess the relative contributions of alkaline chemical components (Fig. 6f). As expected, this ratio during the two dust stages was much higher than that of NDS, indicating the important contribution of dust to alkaline metal ions. The Ca^{2+}/NH_4^+ ratio was higher during P3 (0.15) than during P2 (0.10), which aligned with the findings presented in Section 3.2.

Formatted ...

Formatted: Font: Not Bold

Formatted ...

Formatted: Indent: First line: 2 ch

3.4.2. Distinct formation processes of secondary aerosols between P2 and P3

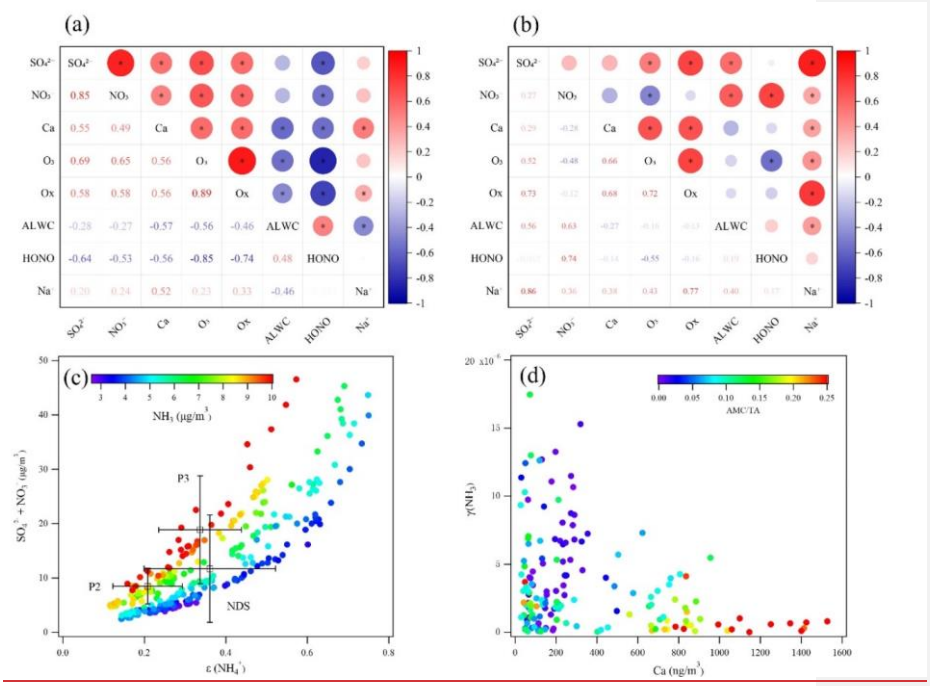

Figure 7. Correlation heatmaps during (a) P2 and (b) P3. (c) The mass concentrations of SO_4^{2-} and NO_3^- as a function of $\varepsilon(NH_4^+)$, with dots colored by the concentration of NH_3. (d) The uptake coefficient of NH_3 (γ_{NH3}) on particles as a function of Ca, with dots colored by the AMC/TA molar ratios. AMC and TA denotes the total molar concentrations of Na^+, K^+, Mg^{2+}, and Ca^{2+} and the total molar concentrations of anions, respectively.

In this section, we further analyze the formation mechanism and key influencing factors of secondary components during P2 and P3. Figure 7a & 7b compare the correlation heatmaps of SO_4^{2-} and NO_3^- with various parameters. During P2, both SO_4^{2-}

Formatted: Subscript

Formatted: Font: Not Bold
Formatted: Font: Not Bold
Formatted: Font: Not Bold
Formatted: Font: Not Bold
Formatted: Font: Not Bold, Subscript
Formatted: Font: Not Bold, Superscript
Formatted: Font: Not Bold
Formatted: Font: Not Bold, Subscript
Formatted: Font: Not Bold, Superscript
Formatted: Font: Not Bold
Formatted: Font: Not Bold
Formatted: Font: Not Bold, Subscript
Formatted: Font: Not Bold, Superscript
Formatted: Font: Not Bold

and NO_3^- displayed the most significant correlations with O_3 and Ox (O_3+NO_2), while even negatively correlated with ALWC. In regard of the obvious ozone enhancement phenomenon as discussed in Section 3.3.1, photochemistry should be the main pathway for the secondary aerosol formation rather than the liquid phase processing. In addition, SO_4^{2-} and NO_3^- also showed moderate correlations with elemental Ca, suggesting that dust acted as a carrier to transport these salts, which can be derived from background minerals in dust (Wu et al., 2022) and dust heterogeneous reactions during the transport (Huang et al., 2010a).

As for P3, it showed a distinctly different correlation heatmap from P2. While SO_4^{2-} still demonstrates a correlation with O3, the relationship between NO_3^- and O_3 (as well as Ox) disappeared. On the contrary, both SO_4^{2-} and NO_3^- show significant correlations with ALWC. During P3, the average RH reached 76%, providing favorable conditions for liquid-phase reactions. Furthermore, by relating NO_3^- and the multiplication of ALWC and NO_2, the correlation coefficient (R^2 = 0.41) was further improved (Figure S4a). Similar results were observed by relating NO_3^- to the multiplication of ALWC and NO_2*O_3*NO_2 (a proxy of N_2O_5, (Huang et al., 2021)) (Figure S4b), confirming the dominant reaction pathway of nitrogen oxides to nitrate via the aqueous phase reactions. As a result, NO_3^- was also strongly correlated with HONO (Figure S4c), typically deriving from the heterogeneous reactions of NO_2 on the surface of moist particles (Alicke et al. (2002).

In addition, unlike P2, both SO_4^{2-} and NO_3^- showed moderate to significant correlations with Na^+. Since neither SO_4^{2-} nor NO_3^- correlated with Ca, it can be inferred that sea salts played a more important role in the transport of air pollutant during the dust backflow over the ocean. To assess whether dust or sea salts participated in the

Formatted ...
Formatted ...
Formatted: Font: Not Bold, Subscript
Formatted: Font: Not Bold
Formatted: Font: Not Bold, Subscript
Formatted: Font: Not Bold
Formatted: Font: Not Bold, Subscript
Formatted: Font: Not Bold
Formatted ...
Formatted: Font: Not Bold
Formatted ...
Formatted ...
Formatted ...
Formatted ...
Field Code Changed
Formatted ...
Field Code Changed
Formatted ...

heterogeneous reactions of secondary aerosol during P3, the ISORROPIA II model was run with different scenarios. Figure S5 shows the model performance for SO_4^{2-}, NO_3^-, NH_4^+, and NH_3 based on the SO_4^{2-}–NO_3^-–NH_4^+–Cl^-–NH_3–HCl–HNO_3 system. After adding Ca^{2+} into this thermodynamic equilibrium system, the correlations between the simulations vs observations for all four species were lowered with different extents (Figure S6). If Na^+ was added into the thermodynamic equilibrium system. the model performance was slightly improved (Figure S7). This corroborated that the heterogeneous reactions on dust were very limited while sea salts were intensively involved in the formation of secondary inorganic aerosols during the dust backflow.

To further explore the influencing factors affecting the formation of secondary inorganic aerosols, we examined the role of NH_3 in different stages, representing by the relationship between the gas-particle partitioning of ammonia ($\varepsilon(NH_4^+)$, defined as the ratio between particle phase ammonia (NH_4^+) and total ammonia ($NH_x = NH_3+NH_4^+$)) and the total acids ($SO_4^{2-} + NO_3^-$). As shown in Figure 7c, it is obvious that the total acids strongly co-varied with $\varepsilon(NH_4^+)$. Higher $\varepsilon(NH_4^+)$ resulted in higher concentrations of secondary aerosols. Moreover, under similar $\varepsilon(NH_4^+)$ conditions, higher NH_3 promoted stronger formation of secondary aerosols. Thus, both NH_3 and $\varepsilon(NH_4^+)$ collectively determined the aerosol formation potential. The mean states of P2, P3, and NDS are compared in Figure 7c. P2 had the lowest $\varepsilon(NH_4^+)$ with the mean value of 0.21, despite the relatively high concentrations of NH3 during this period (7.9 ± 1.0 μg/m^3). The relatively low gas-particle partitioning of ammonia limited the neutralization of the acidic components. In contrast, NH3 during P3 was the highest during the study period (9.8 ± 1.8 μg/m^3), and $\varepsilon(NH_4^+)$ (0.34) was only slightly lower than that during NDS, thus effectively fostering the formation of secondary inorganic

Formatted: Not Highlight
Formatted: Indent: First line: 2 ch
Formatted ...
Formatted ...
Formatted ...
Formatted ...
Formatted ...
Formatted ...
Formatted ...
Formatted: Font: 小四
Formatted ...
Formatted: Font: 小四

aerosols.

To explain this phenomenon, the uptake coefficient of NH_3 (γ_{NH_3}) on particles, which is one of the important parameters affecting the gas-particle partitioning of ammonia, was calculated. Figure 7d shows the decreasing trend of γ_{NH_3} with the increase of dust intensity (using Ca as an indicator). This coincided with a multi-year observational study in Beijing and Shijiazhuang, where γ_{NH_3} obviously increased due to significant decline in alkali earth metal contents from the dust emission sources during 2018 – 2020 (Liu et al., 2022). Thus, this partially explained why $\varepsilon(NH_4^+)$ was relatively low during P2, which was ascribed to the reduced uptake capacity of NH_3 on particles.

The ion balance calculation indicated that the total anions and cations are in ideal equilibrium (Figure S8, regression slope = 0.99, R^2 = 0.99), indicating that both NH_4^+ and alkali metal cations (including Na^+, K^+, Mg^{2+}, and Ca^{2+}) contributed to the neutralization of acids to varying degrees. The ratio of alkali metal cations/total anions (AMC/TA) was used to color the data points in Figure 7d, showing an opposite trend between AMC/TA and γ_{NH_3}. During P2, the mean value of AMC/TA reached 21%, implying that the neutralization of acids by NH_3 had been significantly suppressed, thus explaining `the decrease in the NH_3 uptake coefficient at high dust intensity. In contrast, the AMC/TA ratio decreased to 11% during P3, indicating a reduced competition between NH_3 and the alkali dust components. Finally, we also compared the aerosol pH at different stages, which was 3.2, 3.0, and 2.8 during P2, P3, and NDS, respectively. The relatively high aerosol acidity at P3 and NDS favored the uptake of alkaline gases (Liu et al., 2022), which also contributed to the higher (γ_{NH_3}) at these two stages.

Formatted: Font: 小四, Subscript
Formatted: Font: 小四
Formatted: Font: 小四, Subscript
Formatted: Font: 小四
Formatted: Font: 小四
Formatted: Font: 小四
Formatted: Font: 小四
Formatted: Font: 小四
Formatted: Font: 小四
Formatted: Font: 小四
Formatted: Font: 小四
Formatted: Font: 小四, Subscript
Formatted: Font: 小四
Formatted: Superscript
Formatted: Subscript
Formatted: Superscript
Formatted: Superscript
Formatted: Superscript
Formatted: Superscript
Formatted: Superscript
Formatted: Subscript
Formatted: Subscript
Formatted: Subscript
Formatted: Subscript
Formatted: Subscript

3.4.2. Formation processes of secondary aerosols during P3

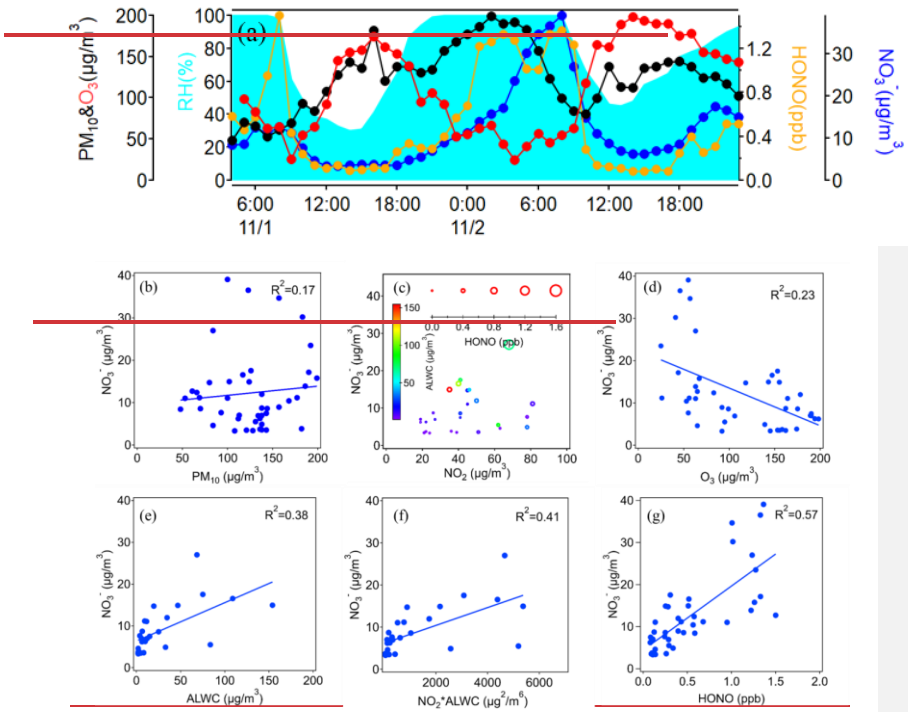

Figure 11. (a) Time series of PM_{10}, NO_3^-, O_3, HONO, and RH during P3. Linear relationship between nitrate and (b) PM_{10}, (c) NO_2, (d) O_3, (e) ALWC, (f) NO_2*AWLC, and (g) HONO.

In this section, the main processes that dominated the formation of secondary aerosols during P3 were probed and compared to P2. Figure 11a shows the time-series of hourly PM_{10}, NO_3^-, O_3, HONO, and RH during P3. It could be visualized that most parameters co-varied relatively consistently to some extent. Different from P2, nitrate showed weak correlation with PM_{10} (Figure 11b), indicating that part of nitrate could be directly transported via the dust transport. Also different from P2, nitrate even showed negative correlation with O_3 (Figure 11d). From Figure 11a, nitrate

~~concentrations were at its troughs during daytime when O_3 peaked. Thus, photochemical reactions didn't play an important role in the formation of nitrate during this stage.~~

~~Figure 11c investigates the conjoint impact of multiple parameters on the formation of nitrate. In general, NO_3^- was more favored under higher NO_2, which was obviously expected as NO_3^- could be either formed by the photochemical oxidation of NO_2 by OH radicals at daytime (Hertel et al., 2012) or produced by hydrolysis of N_2O_5 from the oxidation of NO_2 by O_3 at nighttime (Ge et al., 2017). In addition, the formation of higher NO_3^- was accompanied with higher ALWC and HONO, implying the role of aqueous phase reactions rather than the photochemical reactions. Figure 11e-11g separately investigate the relationship between NO_3^- and various parameters. NO_3^- moderately correlated with ALWC ($R^2 = 0.38$). By relating NO_3^- and the multiplication of ALWC and NO_2, the correlation coefficient ($R^2 = 0.41$) was further improved (Figure 11f), indicating the reaction pathway of NO_2 to nitrate in the aqueous phase. Figure 11g also observed strong correlation between NO_3^- and HONO ($R^2 = 0.57$). Alicke et al. (2002) proposed that the heterogeneous reactions of NO_2 on the surface of moist particles produced both nitrate and HONO, i.e.,~~

~~$$2NO_2+H_2O \rightarrow HONO+HNO_3$$~~

~~Compared to the mean ALWC ($11.8 \pm 17.1 \mu g/m^3$) during P2, ALWC during P3 was much higher of $29.1 \pm 38.0 \mu g/m^3$. This was mainly ascribed to the higher atmospheric water vapor during P3, which was evidently caused by the backflows of oceanic air masses. The different levels of ALWC between P2 and P3 caused divergent role of aqueous processing in the secondary aerosol formation.~~

~~As for sulfate, its temporal variation during P3 was quite different from NO_3^- that~~

it showed no diurnal pattern while presented a gradually increasing trend (Figure 12a). This suggested sulfate had gone through a different formation mechanism from nitrate. SO_4^{2-} correlated strongly with Na^+ (Figure 12e), which can be regarded as the tracer of sea salts. The co-variation of SO_4^{2-} and Na^+ probably suggested that a portion of sulfate was aged and directly transported by the oceanic air masses. Additionally, SO_4^{2-} had weakly positive correlation with O_3 (Figure 12d) and ALWC (Figure 12e), indicating that both gas and aqueous phase processes contributed to the secondary formation of sulfate to some extent. Figure 12a also adds the time series of Ca^{2+}/Ca, which didn't co-vary with either sulfate or nitrate. This probably indicated that the chemical reactions between acidic gaseous precursors and dust mineral components were negligible.

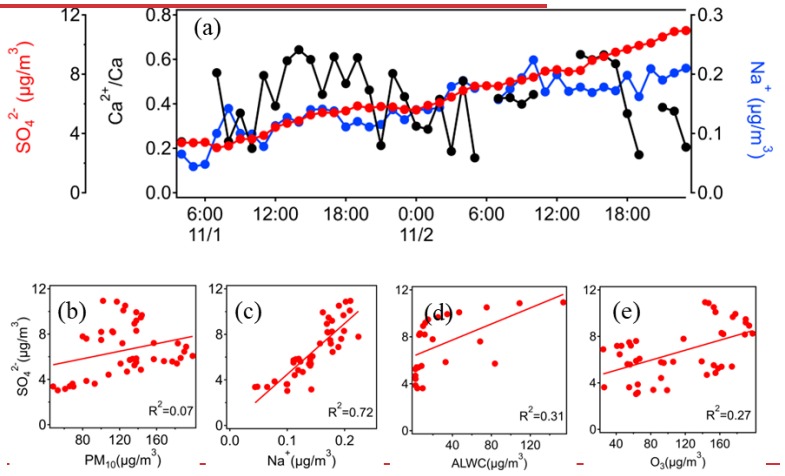

Figure 12. (a) Time-series of sulfate, Na^+, and Ca^{2+}/Ca during P3. Linear between sulfate and (b) PM_{10}, (c) Na^+, (d) O_3, and (e) ALWC.

To assess whether dust or sea salts participated in the heterogeneous reactions of secondary aerosol during P3, the ISORROPIA II model was run with different scenarios. Figure S1 shows the model performance for SO_4^{2-}, NO_3^-, NH_4^+, and NH_3 based on the

~~SO_4^{2-}–NO_3^-–NH_4^+–Cl^-–NH_3–HCl–HNO_3 system. After adding Ca^{2+} into this thermodynamic equilibrium system, the correlations between the simulations vs observations for all four species were lowered with different extents (Figure S2). This indicated that Ca^{2+} was not internally mixed with sulfate and nitrate and probably suggested that the heterogeneous reactions on dust were very limited.~~

~~Then Na^+ was added into the thermodynamic equilibrium system (Figure S3). It could be seen the model performance was slightly improved. The correlation coefficients of the four species were closer to the unity and the regression slopes were also more parallel to the y=x line. This suggested that sea salts were involved in the formation of secondary inorganic aerosols during the dust backflow. This also explained the strong correlation between SO_4^{2-} and Na^+ during P3.~~

~~3.4.3.~~ 3.5. Estimation of transported and secondarily formed particles during P3

As discussed in ~~the~~ previous sections, the ~~sources of~~ aerosols observed during P3 could originate ~~be derived~~ from both aged aerosols transported via the dust backflows and secondary formation. In this section, we aimed to estimate the contribution of transport and secondary formation to the main aerosol species, respectively, based on the simultaneous measurements at the Pudong site and the Lianyungang site. As discussed in Section 3.4.1, Lianyungang acted as an upstream region ~~of~~ where dust ~~transport~~ drifted away~~ing~~ from the mainland. The duration of dust ~~duration~~ observed at Lianyungang was approximately from ~~about~~ 5:00~~,~~ on October 30 to 16:00~~,~~ on October 31, about 46 hours ahead of the dust invasion observed at Pudong (Figure ~~9~~S2).

To assess the extents of transported air pollutants, black carbon (BC) was used as a reference aerosol component. As shown in Figure ~~S4~~S9, one BC pollution episode on

Formatted: Font: (Default) Times New Roman, 小四, Font color: Auto, Pattern: Clear

Formatted: Font: (Default) Times New Roman, 小四, Font color: Auto, Pattern: Clear

Formatted: Font: (Default) Times New Roman, 小四, Font color: Auto, Pattern: Clear

Formatted: Font: (Default) Times New Roman, 小四, Font color: Auto, Pattern: Clear

October 30 at Lianyungang was observed. CorrespondinglyConsistently, another BC pollution episode on November 2 emerged at Pudong on November 2emerged after about 46 hours. Since the air mass trajectory from Lianyungang to Pudong predominantly traversedwas mostly over the ocean, and considering that and BC had has no secondary sources, it could can be reasonably assumed that the differences of BC concentrations between these two sites was were ascribed to the removal processes of particles.

To determine the removal fractions of aerosols during dust transport, we first We further defined the average concentrations of various aerosol components during the preceding previous five hours of the dust at Pudong as their background concentrations. Then, a coefficient k was derived to calculate the removal fractions of aerosols during the dust transport as below.

$$k = \frac{AV_{LYG,BC} - (AV_{PD,BC} - BKG_{PD,BC})}{AV_{LYG,BC}}$$

$AV_{LYG,BC}$ and $AV_{PD,BC}$ represent the average concentration of BC at Lianyungang and Pudong during their respective dust period. $BKG_{PD,BC}$ represents the background concentration of BC at Pudong. By aAssuming that other aerosol species were removed at with a similar efficiency as BC, the amounts of transported aerosol species from Lianyungang to Pudong can be estimated as below.

$$TP_{PD,i} = AV_{LYG,i} \times (1 - k)$$

$TP_{PD,i}$ represents the transported amounts for of aerosol species i. Then, the secondarily formed aerosol species i at Pudong can be calculated as below.

$$SF_{PD,i} = AV_{PD,i} - BKG_{PD,i} - TP_{PD,i}$$

Figure 13 8 shows the results of the transported and the secondarily formed aerosol

Formatted: Font: (Default) Times New Roman, 小四, Font color: Auto, Pattern: Clear

Formatted: Font: (Default) Times New Roman, 小四, Font color: Auto, Pattern: Clear

Formatted: Font: (Default) Times New Roman, 小四, Font color: Auto, Pattern: Clear

Formatted: Font: (Default) Times New Roman, 小四, Font color: Auto, Pattern: Clear

Formatted: Font: (Default) Times New Roman, 小四, Font color: Auto, Pattern: Clear

species during P3. It was calculated that the secondarily formed and transported NO_3^- averaged 6.8μg/m^3 and 4.7μg/m^3, accounting for about 45% and 31% of its total mass concentration, respectively. This was consistent with the earlier analysis ~~above~~ that a considerable portion of nitrate was formed through the aqueous phase secondary formation. In contrast, it was calculated that the transported SO_4^{2-} accounted for about 42% of its total mass concentration, while the secondarily formed SO_4^{2-} was almost negligible. This was also consistent with the phenomenon that SO_4^{2-} correlated significantly with Na^+ (Figure ~~12e~~6b)~~, suggesting most sulfate was aged and transported~~. As for NH_4^+, it exhibited a similar apportionment as~~its origin apportionment was similar to~~ NO_3^- ~~that~~, with the secondarily formed and transported NH_4^+ accounting~~ed~~ for about 35% and 28% of its total mass concentration, respectively. Compared to NO_3^- and NH_4^+, OM was more dominated by transport (57%) while its secondary formation only accounted for about 13%.

Formatted: Font: (Default) Times New Roman, 小四, Font color: Auto, Pattern: Clear

Formatted: Font: (Default) Times New Roman, 小四, Font color: Auto, Pattern: Clear

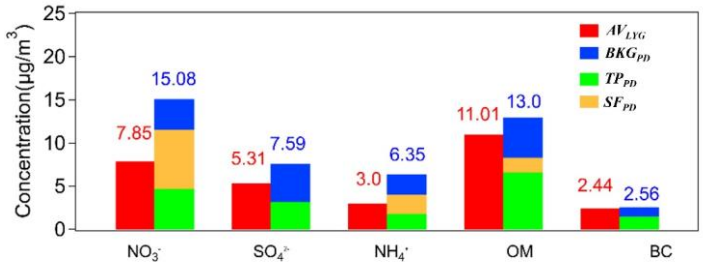

Figure ~~13~~8. The apportioned concentrations of the major aerosol species during P3.

4. Conclusion

During October 29 to November 2, 2019, a long-lasting dust event was observed in Shanghai based on a synergy measurement of near surface air pollutants, aerosol lidar, wind profiling lidar, and air masses trajectory modeling. During the whole dust period, the mean concentrations of $PM_{2.5}$ and PM_{10} reached 53.3 ± 20.5μg/m^3 and 172.4 ± 70.2μg/m^3. Different from most dust events, this dust event was characterized of exceptionally high relative humidity (71 ± 26%) and low wind speed (0.54 ± 0.59m/s). Due to this stagnant synoptic condition, the mean concentrations of main gaseous pollutants such as O_3, SO_2, and NO_2 reached 86.0 ± 47.8μg/m^3, 11.8 ± 3.4μg/m^3, and 63.3 ± 27.9μg/m^3, respectively, even higher than those during the non-dust period.

The dust event was divided into three stages from P1 – P3. P1 was a short dust episode ~~from 4:00 - 13:00, October 29,~~ when wind profiles showed dominant northwest winds from the ground to the altitudes of around 2km, indicating the presence of a strong synoptic system. P2 was a dust episode ~~from 14:00, October 29 to 3:00, November 1,~~ when RH was moderately high of 70 ± 26% and the southeasterlies prevailed with partial air masses from coastal regions. P3 was a rarely observed dust backflow transport episode ~~from 4:00, November 1 to 23:00, November 2~~. The air masses originated from the Shandong Peninsula and the northern region of Jiangsu province, and then migrated over the Yellow Sea and the East China Sea. RH reached the highest of 76 ± 24% among the three stages of the dust event.

During P2, mineral aerosols accounted for 33% in $PM_{2.5}$, the highest among all three stages. Abnormally high O_3 concentrations were observed, much higher than the non-dust days. This was partially due to the weak synoptic system that exerted weak dilution effect on the local air pollutants. ~~Also, part of O_3 could be transported from the high ozone oceanic areas.~~ The ozone lidar observed that the subsidence of dust particles

probably down drafted high-altitude O_3 and also contributed to the high O_3 near the ground. As a result, sulfate and nitrate moderately correlated with O_3 while had almost no correlation with ALWC, indicating that the formation of secondary aerosols during P2 should be mainly promoted via the gas-phase oxidations.

During P3, a special phenomenon of dust backflow was observed and confirmed by various evidences. Two upstream sites (Qingdao and Lianyungang) showed dust occurrences about 48 hours ahead that of Shanghai, consistent with the transport duration of the dust backflow from the Shandong Peninsula to Shanghai over the Yellow Sea and the East China Sea. As a result, ~~T~~the highest Ca^{2+}/Ca ratio ~~of 0.38 ± 0.19 was~~ observed ~~during P3, which should be~~ due to that the lingerer of dust plumes over the open ocean ~~facilitated efficient solubility of calcium~~. ~~In addition~~Moreover, ~~the mass concentrations~~contributions of V and Ni significantly increased, indicating the mixing between dust and marine vessel emissions. ~~The highest Ca^{2+}/Ca ratio of 0.38 ± 0.19 was observed during P3, which should be due to that the lingerer of dust plumes over the open ocean facilitated efficient solubility of calcium.~~ Different from P2, nitrate ~~didn't correlate with O_3, while it was favored under high NO_2 and~~ significantly correlated with ALWC but not with O_3, ~~and strongly correlated with HONO~~, indicating its aqueous-phase ~~the~~ reaction pathway ~~of NO_2 to nitrate in the aqueous phase~~. ~~As for~~Also, sulfate and nitrate exhibited ~~, the~~ moderate to strong correlations with ~~between SO_4^{2-} and~~ Na^+~~-~~, suggesting sea salts as a medium for the heterogeneous reactions. ~~ed that a portion of sulfate was aged and directly transported by the oceanic air masses. The ISORROPIA II modeling added Na^+ into the SO_4^{2-}-NO_3^--NH_4^+-Cl^--NH_3-HCl-HNO_3 system and found the models performances of simulating the major aerosol and gaseous species could be improved. As a~~

~~comparison, the models performances became worse after adding Ca^{2+}. This suggested that sea salts participated in the secondary aerosol formation while dust heterogeneous reactions were limited during P3.~~

By analyzing various chemical tracers, the formation extent of SNA was found much stronger during P3 than during P2. Both NH_3 and $\varepsilon(NH_4^+)$ ($NH_4^+/(NH_3+NH_4^+)$) determined the concentrations of SNA. To explain the relatively high $\varepsilon(NH_4^+)$ values during P3, the uptake coefficient of NH_3 (γ_{NH3}) on particles is calculated. γ_{NH3} negatively varied with the intensity of dust, which were attributed to two factors. Higher contributions of alkali metal components suppressed the neutralization capacity of NH3 on acids, thereby lowering γ_{NH3} during P2. Also, relatively high aerosol pH during P2 didn't facilitate the uptake of NH3 and the subsequent aerosol formation.

Based on a simplifie~~d~~ method, the amounts of transported and secondarily formed particles during P3 were quantified. It was calculated that about 45% and 31% of NO_3^- was contributed by secondary formation and transport, respectively. In contrast, the transported SO_4^{2-} accounted for about 42% of its total mass concentration while the rest was from its background concentration with negligible secondary formation. OM was dominated by transport (57%) while its secondary formation only accounted for about 13%.

Data Availability Statement

All data used in this study can be requested upon the corresponding author (huangkan@fudan.edu.cn).

Formatted: Left

Formatted: Subscript

Author contributions

KH, QF, and YD designed this study. JH, FY, YL, and JC performed data collection. DL and KH performed data analysis and wrote the paper. All have commented on and reviewed the paper.

Competing interests

The authors declare that they have no conflict of interest.

Acknowledgments

This work was financially supported by the National Science Foundation of China (42175119).

References

Alicke, B., Platt, U., and Stutz, J.: Impact of nitrous acid photolysis on the total hydroxyl radical budget during the Limitation of Oxidant Production/Pianura Padana Produzione di Ozono study in Milan, J. Geophys. Res.-Atmos., 107, 18, 10.1029/2000jd000075, 2002.

Ansari, A. S. and Pandis, S. N.: An analysis of four models predicting the partitioning of semivolatile inorganic aerosol components, Aerosol Science And Technology, 31, 129-153, 10.1080/027868299304200, 1999.

Arimoto, R., Ray, B. J., Lewis, N. F., Tomza, U., and Duce, R. A.: Mass-particle size distributions of atmospheric dust and the dry deposition of dust to the remote ocean, J. Geophys. Res.-Atmos., 102, 15867-15874, 10.1029/97jd00796, 1997.

Barkley, A., Olson, N., Prospero, J., Gatineau, A., Panechou, K., Maynard, N., Blackwelder, P., China, S., Ault, A., and Gaston, C.: Atmospheric Transport of North African Dust‐Bearing Supermicron Freshwater Diatoms to South America: Implications for Iron Transport to the Equatorial North Atlantic Ocean, Geophysical Research Letters, 48, 10.1029/2020GL090476, 2021.

Becagli, S., Sferlazzo, D. M., Pace, G., di Sarra, A., Bommarito, C., Calzolai, G., Ghedini, C., Lucarelli, F., Meloni, D., Monteleone, F., Severi, M., Traversi, R., and Udisti, R.: Evidence for heavy fuel oil combustion aerosols from chemical analyses at the island of Lampedusa: a

possible large role of ships emissions in the Mediterranean, Atmos. Chem. Phys., 12, 3479-3492, 10.5194/acp-12-3479-2012, 2012.

Benas, N., Mourtzanou, E., Kouvarakis, G., Bais, A., Mihalopoulos, N., and Vardavas, I.: Surface ozone photolysis rate trends in the Eastern Mediterranean: Modeling the effects of aerosols and total column ozone based on Terra MODIS data, Atmospheric Environment, 74, 1-9, 10.1016/j.atmosenv.2013.03.019, 2013.

Bernard, F., Cazaunau, M., Grosselin, B., Zhou, B., Zheng, J., Liang, P., Zhang, Y., Ye, X., Daële, V., Mu, Y., Zhang, R., Chen, J., and Mellouki, A.: Measurements of nitrous acid (HONO) in urban area of Shanghai, China, Environmental Science and Pollution Research, 23, 5818-5829, 10.1007/s11356-015-5797-4, 2016.

Bozlaker, A., Prospero, J. M., Price, J., and Chellam, S.: Identifying and Quantifying the Impacts of Advected North African Dust on the Concentration and Composition of Airborne Fine Particulate Matter in Houston and Galveston, Texas, J Geophys Res-Atmos, 124, 12282-12300, 10.1029/2019jd030792, 2019.

Cwiertny, D. M., Baltrusaitis, J., Hunter, G. J., Laskin, A., Scherer, M. M., and Grassian, V. H.: Characterization and acid-mobilization study of iron-containing mineral dust source materials, J Geophys Res-Atmos, 113, Artn D05202

10.1029/2007jd009332, 2008.

Dall'Osto, M., Harrison, R. M., Coe, H., and Williams, P.: Real-time secondary aerosol formation during a fog event in London, Atmospheric Chemistry And Physics, 9, 2459-2469, 10.5194/acp-9-2459-2009, 2009.

Fan, Q. Z., Zhang, Y., Ma, W. C., Ma, H. X., Feng, J. L., Yu, Q., Yang, X., Ng, S. K. W., Fu, Q. Y., and Chen, L. M.: Spatial and Seasonal Dynamics of Ship Emissions over the Yangtze River Delta and East China Sea and Their Potential Environmental Influence, Environmental Science & Technology, 50, 1322-1329, 10.1021/acs.est.5b03965, 2016.

Feng, X., Mao, R., Gong, D.-Y., Zhao, C., Wu, C., Zhao, C., Wu, G., Lin, Z., Liu, X., Wang, K., and Sun, Y.: Increased Dust Aerosols in the High Troposphere Over the Tibetan Plateau From 1990s to 2000s, Journal of Geophysical Research: Atmospheres, 125, e2020JD032807, https://doi.org/10.1029/2020JD032807, 2020.

Ge, X. L., He, Y. A., Sun, Y. L., Xu, J. Z., Wang, J. F., Shen, Y. F., and Chen, M. D.: Characteristics and Formation Mechanisms of Fine Particulate Nitrate in Typical Urban Areas in China, Atmosphere, 8, 12, 10.3390/atmos8030062, 2017.

Ginoux, P., Prospero, J. M., Torres, O., and Chin, M.: Long-term simulation of global dust distribution with the GOCART model: correlation with North Atlantic Oscillation, Environmental Modelling & Software, 19, 113-128, https://doi.org/10.1016/S1364-8152(03)00114-2, 2004.

970 Goodman, M. M., Carling, G. T., Fernandez, D. P., Rey, K. A., Hale, C. A., Bickmore, B.
971 R., Nelson, S. T., and Munroe, J. S.: Trace element chemistry of atmospheric deposition along
972 the Wasatch Front (Utah, USA) reflects regional playa dust and local urban aerosols, Chemical
973 Geology, 530, 10.1016/j.chemgeo.2019.119317, 2019.
974 Hammond, D. M., Dvonch, J. T., Keeler, G. J., Parker, E. A., Kamal, A. S., Barres, J. A.,
975 Yip, F. Y., and Brakefield-Caldwell, W.: Sources of ambient fine particulate matter at two
976 community sites in Detroit, Michigan, Atmos. Environ., 42, 720-732,
977 10.1016/j.atmosenv.2007.09.065, 2008.
978 Hertel, O., Skjoth, C. A., Reis, S., Bleeker, A., Harrison, R. M., Cape, J. N., Fowler, D.,
979 Skiba, U., Simpson, D., Jickells, T., Kulmala, M., Gyldenkaerne, S., Sorensen, L. L., Erisman,
980 J. W., and Sutton, M. A.: Governing processes for reactive nitrogen compounds in the European
981 atmosphere, Biogeosciences, 9, 4921-4954, 10.5194/bg-9-4921-2012, 2012.
982 Hilario, M. R. A., Cruz, M. T., Cambaliza, M. O. L., Reid, J. S., Xian, P., Simpas, J. B.,
983 Lagrosas, N. D., Uy, S. N. Y., Cliff, S., and Zhao, Y. J.: Investigating size-segregated sources
984 of elemental composition of particulate matter in the South China Sea during the 2011 Vasco
985 cruise, Atmospheric Chemistry And Physics, 20, 1255-1276, 10.5194/acp-20-1255-2020, 2020.
986 Hsu, S.-C., Lee, C. S. L., Huh, C.-A., Shaheen, R., Lin, F.-J., Liu, S. C., Liang, M.-C., and
987 Tao, J.: Ammonium deficiency caused by heterogeneous reactions during a super Asian dust
988 episode, Journal of Geophysical Research: Atmospheres, 119, 6803-6817,
989 10.1002/2013jd021096, 2014.
990 Huang, K., Fu, J. S., Lin, N.-H., Wang, S.-H., Dong, X., and Wang, G.: Superposition of
991 Gobi Dust and Southeast Asian Biomass Burning: The Effect of Multisource Long-Range
992 Transport on Aerosol Optical Properties and Regional Meteorology Modification, Journal of
993 Geophysical Research: Atmospheres, 124, 9464-9483, https://doi.org/10.1029/2018JD030241,
994 2019.
995 Huang, K., Zhuang, G., Li, J., Wang, Q., Sun, Y., Lin, Y., and Fu, J. S.: Mixing of Asian
996 dust with pollution aerosol and the transformation of aerosol components during the dust storm
997 over China in spring 2007, Journal of Geophysical Research, 115, 10.1029/2009jd013145,
998 2010a.
999 Huang, K., Zhuang, G. S., Li, J. A., Wang, Q. Z., Sun, Y. L., Lin, Y. F., and Fu, J. S.: Mixing
1000 of Asian dust with pollution aerosol and the transformation of aerosol components during the
1001 dust storm over China in spring 2007, J Geophys Res-Atmos, 115, Artn D00k13
1002 10.1029/2009jd013145, 2010b.
1003 Huang, X., Ding, A. J., Gao, J., Zheng, B., Zhou, D. R., Qi, X. M., Tang, R., Wang, J. P.,
1004 Ren, C. H., Nie, W., Chi, X. G., Xu, Z., Chen, L. D., Li, Y. Y., Che, F., Pang, N. N., Wang, H.
1005 K., Tong, D., Qin, W., Cheng, W., Liu, W. J., Fu, Q. Y., Liu, B. X., Chai, F. H., Davis, S. J.,

Zhang, Q., and He, K. B.: Enhanced secondary pollution offset reduction of primary emissions during COVID-19 lockdown in China, Natl Sci Rev, 8, ARTN nwaa137 10.1093/nsr/nwaa137, 2021.

Jeong, G. Y.: Bulk and single-particle mineralogy of Asian dust and a comparison with its source soils, J Geophys Res-Atmos, 113, Artn D02208 10.1029/2007jd008606, 2008.

Ji, Y., Qin, X. F., Wang, B., Xu, J., Shen, J. D., Chen, J. M., Huang, K., Deng, C. R., Yan, R. C., Xu, K. E., and Zhang, T.: Counteractive effects of regional transport and emission control on the formation of fine particles: a case study during the Hangzhou G20 summit, Atmos Chem Phys, 18, 13581-13600, 10.5194/acp-18-13581-2018, 2018.

Jiang, Y., Zhuang, G., Wang, Q., Huang, K., Deng, C., Yu, G., Xu, C., Fu, Q., Lin, Y., Fu, J. S., Li, M., and Zhou, Z.: Impact of mixed anthropogenic and natural emissions on air quality and eco-environment—the major water-soluble components in aerosols from northwest to offshore isle, Air Quality, Atmosphere & Health, 11, 521-534, 10.1007/s11869-018-0557-5, 2018.

Laskin, A., Wietsma, T. W., Krueger, B. J., and Grassian, V. H.: Heterogeneous chemistry of individual mineral dust particles with nitric acid: A combined CCSEM/EDX, ESEM, and ICP-MS study, J Geophys Res-Atmos, 110, Artn D10208 10.1029/2004jd005206, 2005.

Li, T., Wang, Y., Zhou, J., Wang, T., Ding, A. J., Nie, W., Xue, L. K., Wang, X. F., and Wang, W. X.: Evolution of trace elements in the planetary boundary layer in southern China: Effects of dust storms and aerosol-cloud interactions, J Geophys Res-Atmos, 122, 3492-3506, 10.1002/2016jd025541, 2017.

Liang, Y., Liu, Y., Wang, H., Li, L., Duan, Y., and Lu, K.: Regional characteristics of ground-level ozone in Shanghai based on PCA analysis, Acta Scientiae Circumstantiae, 38, 3807-3815, 2018.

Liu, H., Liu, S., Xue, B., Lv, Z., Meng, Z., Yang, X., Xue, T., Yu, Q., and He, K.: Ground-level ozone pollution and its health impacts in China, Atmospheric Environment, 173, 223-230, https://doi.org/10.1016/j.atmosenv.2017.11.014, 2018.

Liu, J., Ding, J., Rexiding, M., Li, X., Zhang, J., Ran, S., Bao, Q., and Ge, X.: Characteristics of dust aerosols and identification of dust sources in Xinjiang, China, Atmospheric Environment, 262, 118651, https://doi.org/10.1016/j.atmosenv.2021.118651, 2021.

Liu, Y. C., Zhan, J. L., Zheng, F. X., Song, B. Y., Zhang, Y. S., Ma, W., Hua, C. J., Xie, J. L., Bao, X. L., Yan, C., Bianchi, F., Petaja, T., Ding, A. J., Song, Y., He, H., and Kulmala, M.: Dust emission reduction enhanced gas-to-particle conversion of ammonia in the North China

Plain, Nat Commun, 13, ARTN 6887
10.1038/s41467-022-34733-4, 2022.
Ma, S. Q., Zhang, X. L., Gao, C., Tong, Q. S., Xiu, A. J., Zhao, H. M., and Zhang, S. C.: Simulating Performance of CHIMERE on a Late Autumnal Dust Storm over Northern China, Sustainability-Basel, 11, ARTN 1074
10.3390/su11041074, 2019.
Malm, W. C., Sisler, J. F., Huffman, D., Eldred, R. A., and Cahill, T. A.: Spatial and seasonal trends in particle concentration and optical extinction in the United States, Journal of Geophysical Research: Atmospheres, 99, 1347-1370, https://doi.org/10.1029/93JD02916, 1994.
Mentel, T. F., Bleilebens, D., and Wahner, A.: A study of nighttime nitrogen oxide oxidation in a large reaction chamber—the fate of NO2, N2O5, HNO3, and O3 at different humidities, Atmospheric Environment, 30, 4007-4020, https://doi.org/10.1016/1352-2310(96)00117-3, 1996.
Nagashima, K., Suzuki, Y., Irino, T., Nakagawa, T., Tada, R., Hara, Y., Yamada, K., and Kurosaki, Y.: Asian dust transport during the last century recorded in Lake Suigetsu sediments, Geophysical Research Letters, 43, 2835-2842, https://doi.org/10.1002/2015GL067589, 2016.
Nenes, A., Pandis, S. N., and Pilinis, C.: ISORROPIA: A new thermodynamic equilibrium model for multiphase multicomponent inorganic aerosols, Aquat. Geochem., 4, 123-152, 10.1023/a:1009604003981, 1998.
Patel, A. and Rastogi, N.: Chemical Composition and Oxidative Potential of Atmospheric PM10 over the Arabian Sea, ACS Earth Space Chem., 4, 112-121, 10.1021/acsearthspacechem.9b00285, 2020.
Perez, N., Pey, J., Reche, C., Cortes, J., Alastuey, A., and Querol, X.: Impact of harbour emissions on ambient PM10 and PM2.5 in Barcelona (Spain): Evidences of secondary aerosol formation within the urban area, Science Of the Total Environment, 571, 237-250, 10.1016/j.scitotenv.2016.07.025, 2016.
Petetin, H., Sciare, J., Bressi, M., Gros, V., Rosso, A., Sanchez, O., Sarda-Estève, R., Petit, J. E., and Beekmann, M.: Assessing the ammonium nitrate formation regime in the Paris megacity and its representation in the CHIMERE model, Atmos. Chem. Phys., 16, 10419-10440, 10.5194/acp-16-10419-2016, 2016.
Shen, L., Zhao, C., Ma, Z., Li, Z., Li, J., and Wang, K.: Observed decrease of summer sea-land breeze in Shanghai from 1994 to 2014 and its association with urbanization, Atmospheric Research, 227, 198-209, https://doi.org/10.1016/j.atmosres.2019.05.007, 2019.
Song, S., Gao, M., Xu, W., Shao, J., Shi, G., Wang, S., Wang, Y., Sun, Y., and McElroy, M. B.: Fine-particle pH for Beijing winter haze as inferred from different thermodynamic equilibrium models, Atmos. Chem. Phys., 18, 7423-7438, 10.5194/acp-18-7423-2018, 2018.

Su, L., Yuan, Z., Fung, J. C. H., and Lau, A. K. H.: A comparison of HYSPLIT backward trajectories generated from two GDAS datasets, Science of The Total Environment, 506-507, 527-537, https://doi.org/10.1016/j.scitotenv.2014.11.072, 2015.

Sun, P., Nie, W., Wang, T., Chi, X., Huang, X., Xu, Z., Zhu, C., Wang, L., Qi, X., Zhang, Q., and Ding, A.: Impact of air transport and secondary formation on haze pollution in the Yangtze River Delta: In situ online observations in Shanghai and Nanjing, Atmospheric Environment, 225, 117350, https://doi.org/10.1016/j.atmosenv.2020.117350, 2020.

Tang, M., Cziczo, D. J., and Grassian, V. H.: Interactions of Water with Mineral Dust Aerosol: Water Adsorption, Hygroscopicity, Cloud Condensation, and Ice Nucleation, Chemical Reviews, 116, 4205-4259, 10.1021/acs.chemrev.5b00529, 2016.

Tang, M. J., Huang, X., Lu, K. D., Ge, M. F., Li, Y. J., Cheng, P., Zhu, T., Ding, A. J., Zhang, Y. H., Gligorovski, S., Song, W., Ding, X., Bi, X. H., and Wang, X. M.: Heterogeneous reactions of mineral dust aerosol: implications for tropospheric oxidation capacity, Atmos Chem Phys, 17, 11727-11777, 10.5194/acp-17-11727-2017, 2017.

Tian, R., Ma, X., Sha, T., Pan, X., and Wang, Z.: Exploring dust heterogeneous chemistry over China: Insights from field observation and GEOS-Chem simulation, Science of The Total Environment, 798, 149307, https://doi.org/10.1016/j.scitotenv.2021.149307, 2021.

Vicars, W. C. and Sickman, J. O.: Mineral dust transport to the Sierra Nevada, California: Loading rates and potential source areas, Journal of Geophysical Research, 116, 10.1029/2010jg001394, 2011.

Wang, G., Chen, J., Xu, J., Yun, L., Zhang, M., Li, H., Qin, X., Deng, C., Zheng, H., Gui, H., Liu, J., and Huang, K.: Atmospheric processing at the sea-land interface over the South China Sea: secondary aerosol formation, aerosol acidity, and role of sea salts, Journal of Geophysical Research: Atmospheres, n/a, e2021JD036255, https://doi.org/10.1029/2021JD036255,

Wang, G. C., Chen, J., Xu, J., Yun, L., Zhang, M. D., Li, H., Qin, X. F., Deng, C. R., Zheng, H. T., Gui, H. Q., Liu, J. G., and Huang, K.: Atmospheric Processing at the Sea-Land Interface Over the South China Sea: Secondary Aerosol Formation, Aerosol Acidity, and Role of Sea Salts, J. Geophys. Res.-Atmos., 127, 10.1029/2021jd036255, 2022a.

Wang, G. H., Cheng, C. L., Huang, Y., Tao, J., Ren, Y. Q., Wu, F., Meng, J. J., Li, J. J., Cheng, Y. T., Cao, J. J., Liu, S. X., Zhang, T., Zhang, R., and Chen, Y. B.: Evolution of aerosol chemistry in Xi'an, inland China, during the dust storm period of 2013-Part 1: Sources, chemical forms and formation mechanisms of nitrate and sulfate, Atmospheric Chemistry And Physics, 14, 11571-11585, 10.5194/acp-14-11571-2014, 2014.

Wang, H. C. and Lu, K. D.: Determination and Parameterization of the Heterogeneous Uptake Coefficient of Dinitrogen Pentoxide (N2O5), Prog Chem, 28, 917-933,

10.7536/Pc151225, 2016.

Wang, J. J., Zhang, M. G., Bai, X. L., Tan, H. J., Li, S., Liu, J. P., Zhang, R., Wolters, M. A., Qin, X. Y., Zhang, M. M., Lin, H. M., Li, Y. N., Li, J., and Chen, L. Q.: Large-scale transport of PM2.5 in the lower troposphere during winter cold surges in China, Sci Rep, 7, 10, 10.1038/s41598-017-13217-2, 2017.

Wang, L., Du, H., Chen, J., Zhang, M., Huang, X., Tan, H., Kong, L., and Geng, F.: Consecutive transport of anthropogenic air masses and dust storm plume: Two case events at Shanghai, China, Atmospheric Research, 127, 22-33, https://doi.org/10.1016/j.atmosres.2013.02.011, 2013.

Wang, N., Zheng, P., Wang, R., Wei, B., An, Z., Li, M., Xie, J., Wang, Z., Wang, H., and He, M.: Homogeneous and heterogeneous atmospheric ozonolysis of acrylonitrile on the mineral dust aerosols surface, Journal of Environmental Chemical Engineering, 9, 106654, https://doi.org/10.1016/j.jece.2021.106654, 2021.

Wang, Q., Wang, X., Huang, R., Wu, J., Xiao, Y., Hu, M., Fu, Q., Duan, Y., and Chen, J.-M.: Regional Transport of PM 2.5 and O 3 Based on Complex Network Method and Chemical Transport Model in the Yangtze River Delta, China, Journal of Geophysical Research: Atmospheres, 127, 10.1029/2021JD034807, 2022b.

Wang, Z., Pan, X. L., Uno, I., Chen, X. S., Yamamoto, S., Zheng, H. T., Li, J., and Wang, Z. F.: Importance of mineral dust and anthropogenic pollutants mixing during a long-lasting high PM event over East Asia, Environ. Pollut., 234, 368-378, 10.1016/j.envpol.2017.11.068, 2018.

Wang, Z. L., Huang, X., Wang, N., Xu, J. W., and Ding, A. J.: Aerosol-Radiation Interactions of Dust Storm Deteriorate Particle and Ozone Pollution in East China, J Geophys Res-Atmos, 125, ARTN e2020JD033601

10.1029/2020JD033601, 2020.

West, J. J., Ansari, A. S., and Pandis, S. N.: Marginal PM25: Nonlinear Aerosol Mass Response to Sulfate Reductions in the Eastern United States, Journal of the Air & Waste Management Association, 49, 1415-1424, 10.1080/10473289.1999.10463973, 1999.

Wu, C., Zhang, S., Wang, G., Lv, S., Li, D., Liu, L., Li, J., Liu, S., Du, W., Meng, J., Qiao, L., Zhou, M., Huang, C., and Wang, H.: Efficient Heterogeneous Formation of Ammonium Nitrate on the Saline Mineral Particle Surface in the Atmosphere of East Asia during Dust Storm Periods, Environmental Science & Technology, 54, 15622-15630, 10.1021/acs.est.0c04544, 2020.

Wu, F., Cheng, Y., Hu, T. F., Song, N., Zhang, F., Shi, Z. B., Ho, S. S. H., Cao, J. J., and Zhang, D. Z.: Saltation-Sandblasting Processes Driving Enrichment of Water- Soluble Salts in Mineral Dust, Environ Sci Tech Let, 9, 921-928, 10.1021/acs.estlett.2c00652, 2022.

Xie, S. D., Yu, T., Zhang, Y. H., Zeng, L. M., Qi, L., and Tang, X. Y.: Characteristics of PM10, SO2, NO, and O-3 in ambient air during the dust storm period in Beijing, Sci Total Environ, 345, 153-164, 10.1016/j.scitotenv.2004.10.013, 2005.

Xu, J., Chen, J., Zhao, N., Wang, G. C., Yu, G. Y., Li, H., Huo, J. T., Lin, Y. F., Fu, Q. Y., Guo, H. Y., Deng, C. R., Lee, S. H., Chen, J. M., and Huang, K.: Importance of gas-particle partitioning of ammonia in haze formation in the rural agricultural environment, Atmospheric Chemistry and Physics, 20, 7259-7269, 10.5194/acp-20-7259-2020, 2020.

Xu, P., Zhang, J. K., Ji, D. S., Liu, Z. R., Tang, G. Q., Hu, B., Jiang, C. S., and Wang, Y. S.: Evaluating the Effects of Springtime Dust Storms over Beijing and the Associated Characteristics of Sub-Micron Aerosol, Aerosol Air Qual Res, 17, 680-692, 10.4209/aaqr.2016.05.0195, 2017.

Yang, Y., Wang, Z. L., Lou, S. J., Xue, L., Lu, J. P., Wang, H. Y., Wang, J. D., Ding, A. J., and Huang, X.: Strong ozone intrusions associated with super dust storms in East Asia, Atmos Environ, 290, ARTN 119355

10.1016/j.atmosenv.2022.119355, 2022.

Yu, S. C., Dennis, R., Roselle, S., Nenes, A., Walker, J., Eder, B., Schere, K., Swall, J., and Robarge, W.: An assessment of the ability of three-dimensional air quality models with current thermodynamic equilibrium models to predict aerosol NO3, J. Geophys. Res.-Atmos., 110, 10.1029/2004jd004718, 2005.

Zhang, D., Iwasaka, Y., Shi, G., Zang, J., Hu, M., and Li, C.: Separated status of the natural dust plume and polluted air masses in an Asian dust storm event at coastal areas of China, Journal of Geophysical Research (Atmospheres), 110, D06302, 10.1029/2004jd005305, 2005.

Zhang, S. P., Xing, J., Sarwar, G., Ge, Y. L., He, H., Duan, F. K., Zhao, Y., He, K. B., Zhu, L. D., and Chu, B. W.: Parameterization of heterogeneous reaction of SO2 to sulfate on dust with coexistence of NH3 and NO2 under different humidity conditions, Atmos Environ, 208, 133-140, 10.1016/j.atmosenv.2019.04.004, 2019.

Zhang, X. L., Wu, G. J., Zhang, C. L., Xu, T. L., and Zhou, Q. Q.: What is the real role of iron oxides in the optical properties of dust aerosols?, Atmos Chem Phys, 15, 12159-12177, 10.5194/acp-15-12159-2015, 2015.

Zhao, D., Xin, J., Wang, W., Jia, D., Wang, Z., Xiao, H., Liu, C., Zhou, J., Tong, L., Ma, Y., Wen, T.-X., Wu, F.-K., and Wang, L.: Effects of the sea-land breeze on coastal ozone pollution in the Yangtze River Delta, Science of The Total Environment, 807, 10.1016/j.scitotenv.2021.150306, 2021.

Zheng, G. J., Duan, F. K., Su, H., Ma, Y. L., Cheng, Y., Zheng, B., Zhang, Q., Huang, T., Kimoto, T., Chang, D., Poschl, U., Cheng, Y. F., and He, K. B.: Exploring the severe winter haze in Beijing: the impact of synoptic weather, regional transport and heterogeneous reactions,

1186 Atmos Chem Phys, 15, 2969-2983, 10.5194/acp-15-2969-2015, 2015.
1187 Zheng, Y., Zhao, T., Che, H., Liu, Y., Han, Y., Liu, C., Xiong, J., Liu, J., and Zhou, Y.: A
1188 20-year simulated climatology of global dust aerosol deposition, Science of The Total
1189 Environment, 557-558, 861-868, https://doi.org/10.1016/j.scitotenv.2016.03.086, 2016.
1190